Quantifying nanotherapeutics penetration using hydrogel based microsystem as a new 3D *in-vitro* platform

Saba Goodarzi[1], Audrey Prunet[1], Fabien Rossetti[1], Olivier Tillement[1], Erika Porcel[2], Sandrine Lacombe[2], Ting-Di Wu[3,4], Jean-Luc Guerquin-Kern[3,4], Hélène Delanoë-Ayari[1], François Lux[1,5], Charlotte Rivière[1,5*]

[1] Institut Lumière Matière, UMR5306, Université Claude Bernard Lyon1-CNRS, Université de Lyon 69622 Villeurbanne Cedex, France

[2] Université Paris-Saclay, CNRS, Institut des Sciences Moléculaires d'Orsay, 91405, Orsay, France

[3] Institut Curie, Université PSL, Paris, France

[4] Université Paris-Saclay, CNRS UMS2016, INSERM US43, Multimodal Imaging Center, Orsay, France

[5] Institut Universitaire de France (IUF)

*corresponding author : charlotte.riviere@univ-lyon1.fr

Abstract [350 words max]

Despite progress in therapeutic strategies and understanding of cancer cell biology, there is a large attrition of promising therapeutics into the clinic. One predominant reason is the huge gap between 2D *in-vitro* assays used for drug screening, and the *in-vivo* 3D-physiological environment. This is particularly important for a specific category of emerging therapeutics: nanoparticles. The lack of physiological context hampered reliable predictions for the route and accumulation of those nanoparticles *in-vivo*. For such nanotherapeutics, Multi-Cellular Tumour Spheroids (MCTS) is emerging as a good alternative *in-vitro* model. However, the classical approaches to produce MCTS suffer from low yield, poor reproducibility and slow process, while spheroid-on-chip set-ups developed so far require a microfluidic practical knowledge difficult to transfer to a cell biology laboratory.

We present here a simple yet highly flexible 3D-model microsystem consisting of agarose-based micro-wells. Fully compatible with the multi-well plates format conventionally used in cell biology, our simple process enables the formation of hundreds of reproducible spheroids in a single pipetting. It is compatible with live high-resolution optical microscopy and provides a user-friendly platform for in-situ immunostaining.

As a proof-of-principle of the relevance of such *in-vitro* platform for the evaluation of nanoparticles, the aim of this study was to analyse the kinetic and localization of nanoparticles within colorectal cancer cells (HCT-116) MCTS. The nanoparticles chosen are sub-5 nm ultrasmall nanoparticles made of polysiloxane and gadolinium chelates that can be visualized in MRI and confocal microscopy (AGuIX®, currently implicated in clinical trials as effective radiosensitizers for radiotherapy). We show that the amount of AGuIX® nanoparticles within cells is largely different in 2D and 3D. Using our flexible agarose-based microsystems, we are able to resolve spatially and temporally the penetration and distribution of AGuIX® nanoparticles within tumour spheroids. The nanoparticles are first found in both extracellular and intracellular space of spheroids, within lysosomes compartment. While the extracellular part is washed away after few days, we evidenced trafficking of AGuIX® nanoparticles that are also found within mitochondria. Our agarose-based microsystem appears hence as a promising 3D *in-vitro* platform for investigation of nanotherapeutics transport, ahead of *in-vivo* studies.

Keywords

Hydrogel-based microsystem, High Content Optical Imaging, nanotherapeutics, Multicellular tumour spheroids (MCTS).

Introduction

There is an ongoing effort to develop efficient therapeutics for cancer treatment including nano-drugs and nanoparticles, nevertheless, the clinical translation of these therapeutics has to overcome numerous challenges from early stages of development to a successful translation [1,2]. Currently, the standard pipeline for drug development is the following: (1) efficacy tests on 2D *in-vitro* assays, (2) and on rodent *in-vivo* models, (3) regulatory toxicity tests on two animal species, (4) clinical trials.

However, 2D *in-vitro* assays do not replicate the 3D-physiological environment encountered by the cells *in-vivo*. That could be the underlying reason of the high rate of clinical failure in development of new drugs. On the other hand, there is also a rising questioning of the economical and ethical relevance of rodent animal models, in particular because such models are not fully representative of human specificity [3]. Getting as close as possible to the *in-vivo* situation in *in-vitro* models is a key issue to truly understand and control cancer cell response, accompanied by reduction in animal usage. For the pharmaceutical industry, tackling this issue will enable better identification of relevant therapeutics by performing relevant screening on 3D models. For precision medicine, it will help physicians to adjust the therapeutic treatment, in complement of current clinical analysis [2,4]. For fundamental research, it will allow deciphering cell response in a truly relevant context.

Many approaches have been developed during the past decade to set-up various organ-on-a-chip or tumour-on-a-chip devices, integrating many different *in-vivo* features in a miniaturized *in-vitro* format [5,6]. This is particularly important for a specific category of emerging therapeutics: nanotherapeutics that are used as drug carriers or therapeutic agents to selectively kill cancer cells [7]. The presence of different physiological barriers such as cell-cell compaction, tumour heterogeneity, the presence of a dense extracellular matrix along with various cancer-associated cells, will decrease the concentration of nanotherapeutics effectively reaching the targeted tumour [8,9]. The lack of such physiological context hampered reliable predictions for the route and accumulation of those nanoparticles *in-vivo* [10] and is a major blocking point for the efficient development of such novel therapeutic approaches [11].To move beyond the classical 2D-plastic dishes, different 3D *in-vitro* models have been developed to try to better replicate *in-vivo* complexity of tumour microenvironment [12]. Among them, Multi-Cellular Tumour Spheroids (MCTS) recapitulate many tumour features including 3D cellular architecture, cellular heterogeneity, signalling pathways and in large spheroids (> 500 µm in diameter) physiochemical gradient similar to real *in-vivo* tumour micrometastasis[13–15] representing a good alternative *in-vitro* model for nanotherapeutics [14–17].

MCTS could be prepared with various techniques[13] such as using non-adherent surfaces [18], spinner flasks [19] or hanging drop methods [20]. Emerging attempts to integrate spheroids in microfluidic set-ups open up new possibilities to deal with the poor reproducibility, low yield and slow process of the classical approach [21,22]. However, such spheroid-on-chip approaches require a microfluidic practical knowledge that is difficult to transfer to a cell biology laboratory.

In addition, the polymeric materials classically used for such devices (Polydimethylsiloxane -PDMS) suffers from major limitations, precluding its usage for efficient drug screening in physiological conditions [23]: large absorption of therapeutics [24,25] (resulting in the underestimation of cell response to drugs), impermeability to small water-soluble molecules (leading to fast-medium conditioning if

continuous flow is not provided otherwise), rigidity several orders of magnitude larger than physiological rigidity (MPa vs kPa range *in-vivo* [26]).

To go beyond PDMS and its limitations, hydrogel-based micro-wells devices have been considered [27,28]. Hydrogels are network of cross-linked polymers with tuneable physical properties and high capacity of water retaining and inter connected pores enabling free diffusion of O_2, nutrient and metabolic wastes, which make them favourable alternatives in micro-system applications. Various techniques using natural or synthetic hydrogels for multicellular tumour spheroids formation, have been developed [28–33]. However, none of these set-ups meets all the criteria required for long-term time-lapse analysis (i.e. compatibility with high-resolution video-microscopy, efficient medium and oxygen renewal, *in-situ* immunostaining/drug application, no reduction of the available drug dose, easy cell retrieval for further standard molecular analyses), within a physiological stiffness range.

We present here a simple yet highly flexible 3D-model microsystem consisting of agarose-based micro-wells. This hydrogel with tuneable rigidity and great integrity presents several advantages making it a suitable biomaterial in cell studies [34,35]. The tuneable mechanical properties of the agarose can reproduce the *in-vivo* microenvironment stiffness. Its porous nature enables the free diffusion of salt and small molecules (size<30 nm in 2% agarose [36], which is the case for most proteins). Our simple process enables the formation of hundreds of reproducible spheroids in a single pipetting, and its compatibility with multi-well plates format conventionally used in cell biology can accelerate the screening of drugs in comparison with conventional 3D models. Of note, these micro-wells can also be manufactured on coverslips, opening up the possibility for live high-resolution optical microscopy. In addition, the hydrogel-based micro-wells provides a user-friendly platform for *in-situ* immunostaining, and can be used for in-depth analysis of cell phenotypic modifications after drug treatment.

As a proof-of-principle of the relevance of such *in-vitro* platform for the evaluation of nanoparticles screening, the aim of this study was to analyse the kinetic and localization of these nanoparticles within colorectal cancer cells (HCT-116) multicellular tumor spheroids. The nanoparticles chosen for this proof-of-concept study are sub-5 nm ultrasmall nanoparticles made of polysiloxane and gadolinium chelates that can be visualized in MRI and confocal microscopy (after functionalization by Cy 5.5, a near infrared fluorophore). These nanoparticles, called AGuIX® are effective radiosensitizers for radiotherapy [37] and are now implicated in three clinical trials associating radiotherapy with AGuIX® for treatment of multiple brain metastases by whole brain radiation therapy (NanoRad 2, Phase II, multicentric), stereotactic radiosurgery (NanoStereo, Phase II, multicentric) and cervical cancer (Phase Ib, Gustave Roussy). Nanoparticles-cell interactions and internalization pathways of these nanoparticles have been assessed *in-vitro* in 2D [38], but never in 3D multicellular tumour spheroids.

We show in this study that the amount of AGuIX® nanoparticles within cells is largely different in 2D and 3D. Using our flexible agarose-based microsystem, we are able to resolve spatially and temporally the penetration and distribution of AGuIX® nanoparticles within tumour spheroids. The nanoparticles are first found in both extracellular and intracellular space of spheroids, within lysosomes compartment. While the extracellular part is washed away after few days, we evidenced trafficking of AGuIX® nanoparticles that are also found within mitochondria. Our agarose-based microsystem appears hence as a promising 3D *in-vitro* platform for investigation of nanotherapeutics transport, ahead of *in-vivo* studies.

126 ## Materials and Methods

127 ### *Hydrogel based microsystem*

128 Hydrogel based microsystems made of agarose were synthesized by polydimethylsiloxane (PDMS)
129 replica moulds, prepared using silicon wafer moulds made by classical photolithography technique.
130 Agarose solution was prepared by mixing ultra-pure agarose powder (Invitrogen™) with deionized
131 water followed by dissolution of agarose in autoclave at 121°C for 15 minutes. The agarose solution
132 was deposited on a warmed PDMS mould (at 78°C) and a coverslip was then placed on top of the drop
133 of agarose so that it spreads with a constant thickness. After agarose gelation into the desired shape,
134 the coverslip was removed and the moulded agarose microwells were cut to fit in the wells of a 24
135 multi-well plate. The microwells were then placed in a 24-multi well plate and keep hydrated with PBS
136 (1mL/well). The plate was UV-sterilized (8 W, 254 nm) for 20 min on opened and closed state and keep
137 at 4°C until used. The day before each experiment, PBS was replaced by culture medium and let to
138 diffuse within each microwell by overnight incubation at 37°C before cell seeding.

139 ### *Colorectal cancer cell line, HCT116 and culture condition*

140 HCT116 colorectal carcinoma (CCL-247) cell line was purchased from the American Type Culture
141 Collection (ATCC, Virginia, USA). All cells were cultured in Dulbecco's Modified Eagle's medium (DMEM-
142 Glutamax, Gibco™), supplemented with 10% of heat-inactivated Fetal Bovine Serum (FBS; Sigma, St.
143 Louis, Missouri, US), 100 units/100 µg of penicillin/streptomycin (Gibco™).
144 Routinely, the HCT116 cell line cells were grown in T-25 cell culture flasks and were placed in the
145 incubator at 37°C with a 5% CO_2 atmosphere. The culture medium was changed regularly, and the cell
146 passage was carried out at 70% confluency every 3 days. The cell passage was performed using
147 recombinant cell-dissociation enzyme (TrypLE, Gibco™) to detach cells followed by neutralizing with
148 culture medium. The cell suspension was centrifuged at 1000 rpm for 5 min, the supernatant was
149 discarded and the cell pellet was resuspended in 1 mL. The number of cells was counted with a
150 Neubauer chamber, and final cell volume was adjusted to reach the desired cell concentration.

151 ### *Multicellular tumour spheroids*

152 Multicellular tumour spheroids of HCT116 cells were formed in 24-well plates containing agarose
153 microwells in each well. After trypsinization and centrifugation, 120000 cells in 1 mL complete medium
154 was added in each well (containing each 1 microsystem). To encourage and accelerate cell aggregation,
155 the 24-wells plate was agitated for 15 minutes in the incubator at 37°C and 5% CO_2. After 4 hours, the
156 plate was rinsed with fresh medium to remove cells that did not reach the micro-wells. After 2 days,
157 spheroids are ready for incubation with drugs or nanoparticles.

158 ### *Monolayer cell culture*

159 After trypsinization and centrifugation of HCT116 cells in culture, a cell suspension with 120000 cells
160 per ml concentration was prepared. The cell suspension was added to tissue-treated coverslip plates
161 (either 300 µL in 8-wells Ibidi® or 2mL in 12-wells plate). Cells were incubated with nanoparticles 48h
162 after cell seeding.

163 ### *Gadolinium based nanoparticles (AGuIX®) conjugated to Cy5.5*

164 The gadolinium-based nanoparticles (AGuIX®) synthesized by NH TherAguix (Lyon, France) are
165 composed of a polysiloxane matrix surrounded by covalently bound DOTAGA (Gd) ((1,4,7,10-
166 tetraazacyclodode-cane-1-glutaric acid-4,7,10-triacetic acid)-Gd). The synthesis process is already
167 described in the literature [39]. Briefly, AGuIX® nanoparticles are composed of a polysiloxane network

168 surrounded by Gd chelates. The chemical composition of AGuIX® nanoparticles is ($GdSi_{6.5}N_6C_{25}O_{21}H_{42}$,
169 $10H_2O)_n$ with a molar mass around 10 kDa. The hydrodynamic diameter of the AGuIX® nanoparticles is
170 close to 5 nm; and the AGuIX® nanoparticles are characterized by a zeta potential of 9.0 ± 5.5 mV at pH
171 7.2. These AGuIX® nanoparticles were further conjugated to Cyanine 5.5 fluorophore to make these
172 nanoparticles detectable by confocal fluorescence microscope. They are referred as AGuIX® -Cy5.5
173 nanoparticles in the rest of the article.

174 ***Incubation of cells with AGuIX®-Cy5.5 nanoparticles***

175 To incubate multicellular tumour spheroids and monolayer cells with AGuIX® -Cy5.5 nanoparticles, an
176 intermediate solution of AGuIX® -Cy5.5 nanoparticles with 100 mM concentration of Gd was prepared
177 in distilled-water. From this intermediate solution, just before the incubation with cells, AGuIX® -Cy5.5
178 solutions were prepared in fresh DMEM with Gd concentrations of 0,8, 1,5 and 2 mM respectively. The
179 Multicellular tumour spheroids in all microsystems of a 24-wells plate were incubated with 1 mL of
180 AGuIX® -Cy5.5 nanoparticles solution. For cell monolayers, an Ibidi® 8-wells plate or a 12-wells plate
181 was used, and cells were incubated with 200 µL or 2 mL AGuIX® -Cy5.5 solution, respectively.

182 ***Inductively coupled plasma-mass spectrometry (ICP-MS)***

183 Concentrations of gadolinium were analysed using a validated inductively coupled plasma-mass
184 spectrometry (ICP-MS). To prepare samples for this analysis, spheroids and monolayer cultured cells
185 were incubated with AGuIX®-Cy5.5 nanoparticles with 0.8, 1.5 and 2 mM concentration in Gd for 24
186 hours. After incubation, spheroids were rinsed three times with PBS for 15 min each and dissociate
187 using Trypsin + EDTA (Gibco). The number of cells in each microwells was evaluated using a Neubaeur
188 chamber. The cell suspensions in trypsin + EDTA of each sample were then centrifuged (3000 rpm for
189 5 min), the supernatants discarded and cells pellets were dissolved in 150 µl HNO_3 69% (ROTH) at 80°
190 C for 3h. The volume of samples was adjusted to 10 mL by adding ultra-pure water and Gd
191 concentration in each sample was measured using ICP-Mass Spectrometer (PerkinElmer, NexION®
192 2000). A similar procedure was used for monolayer cell culture (the cells were rinsed three times with
193 PBS for 5 min each and detached using trypsin (Gibco).
194 The mean value of cells volume was calculated by measuring the cell diameter after detaching or
195 dissociation using bright field microscopy followed by image processing using ImageJ. Accordingly, Gd
196 concentrations obtained by ICP-MS measurements were divided by the average cell volume calculated.

197 ***Localization of nanoparticles: Fixation, permeabilization and immunostaining.***

198 First, cell nuclei and actin filaments in cytoskeleton were labelled. After incubation with AGuIX® -Cy5.5
199 nanoparticles, spheroids were rinsed three times with PBS, 5 min each, they were then fixed in
200 paraformaldehyde (4%) for 20 minutes and permeabilized using 0.1% Triton X-100 (Acros) for 10
201 minutes. After blocking with 3% bovine serum albumin (BSA, Sigma-Aldrich) for 20 minutes, samples
202 were incubated with phalloidin-546 solution (Invitrogen™, A22283, 1:50) in PBS containing nucgreen™-
203 Dead 488 (Invitrogen™, R37109, 1 drop/5ml) at 4°C overnight. The procedure ended with rinsing
204 spheroids three times with PBS, 5 min each.
205 In a second series of experiments, to find out the precise intracellular localization of AGuIX® -Cy5.5
206 nanoparticles, three antibodies : EEA1 for early endosomes (CellSignaling Technology, #3288), AIF for
207 mitochondria (CellSignaling Technology, # 5318) and LAMP-1 for lysosomes (CellSignaling Technology,
208 #9091) have been used to label the main cell compartments. After fixation in paraformaldehyde (4%)
209 for 20 min and rinsing with PBS, three time, 5 min each, according to the protocol proposed by the
210 manufacture, cells were blocked in the buffer (PBS/ 5% BSA/ 0.3% Triton™ X-100) for 60 min, and were

211 rinsed with PBS, three times, 5 min each. Three samples, either spheroids in microwells, either cell
212 monolayer in Ibidi plates were incubated with EEA1 (1:100), AIF (1:400) and LAMP1 (1:200) in the
213 buffer (PBS/ 1% BSA/ 0.1% Triton™ X-100) overnight.
214 The incubation buffers were aspirated and cells were rinsed with PBS three times for 5 min each. For
215 the secondary antibody, Goat-anti rabbit IgG-Alexa 555 (Invitrogen™, A21428, 1:500, diluted in PBS/
216 1% BSA/ 0.1% Triton™ X-100) was used. All samples were then incubated with nucgreen™ Dead 488
217 (Invitrogen™, 1 drop/5 ml) overnight for spheroids and 4 hours for cell monolayers. In the last step,
218 they were rinsed with PBS, three times, 5 min each.

219 ***Confocal fluorescence microscopy***

220 Image acquisitions of spheroids and cell monolayers were carried out with a confocal microscope
221 (Leica SP5) using either a 20X dry objective (NA= 0.7), a 25X water immersion objective (NA=0.95), or
222 a 40X oil immersion objective (NA=1.25). Image acquisitions in Z direction was performed using a 1 µm
223 z-step. Automatic image acquisitions for a large number of spheroids were performed (about 4 hours
224 for 30 spheroids using excitation laser 633 nm with 30% power for AGuIX® nanoparticles).

225 ***Spheroids Clarification***

226 Optical imaging of three-dimensional biological samples can be performed using confocal fluorescence
227 microscopy which images these 3D samples via optical sectioning. However this technique faces
228 several limitations including, light scattering, attenuation of photon due to light absorption and local
229 refractive index differences limiting the light penetration depth [40]. Many different clarification
230 techniques have been developed to overcome such issues [41,42]. In the current study, the clearing
231 efficiency of two methods has been analysed using nucgreen™ signals in HCT116 spheroids: RapiClear
232 1.52 (SunjinLab) and Glycerol [43]. Based on the quantification of fluorescence intensities (**Fig.SI 1**),
233 clarification with glycerol/PBS (80%/20%) has been chosen to clear spheroids in this study.
234 The solution for clarifying spheroids was prepared by mixing glycerol (99.5%, VWR Chemicals) with PBS
235 by the ratio of (80%/20%). A fresh solution was prepared for every experiment. To clarify spheroids,
236 primarily after fixation they were incubated in glycerol solution for 24 h and then the microsystems
237 were transferred to iSpacer (2x0.5mm deep, SunJin Lab) to incubate with fresh glycerol solution and
238 sealed with coverslips to be prepared for image acquisition.

239 ***Image processing***

240 Images obtained by confocal fluorescence microscopy were analysed using a dedicated routine in
241 Matlab. While spheroids are imaged using optical sectioning in Z direction, it is useful to quantify the
242 average signal intensity along the radius of each spheroid.
243 To do this, the entire surface of each spheroid, at each imaging depth were first segmented using the
244 intensity signals coming from every nucleus (labelled with nucgreen™-488). From this segmentation,
245 the segmented spheroids were first fitted into a perfect circle for each imaging depth, followed by
246 fitting each spheroid into a perfect sphere. By changing the coordinates of analysis from Cartesian
247 coordinates (xyz) to the spherical coordinates (R, theta, phi), the mean intensity of AGuIX®-Cy5.5
248 nanoparticles can be averaged along theta and phi angles. The obtained averaged intensity is
249 normalised with the maximum averaged-intensity obtained and plotted as a function of the distance
250 from the periphery.
251 For cell monolayers, the maximum Z-projection of each field of view imaged by confocal microscopy
252 (obtained by image J) is used and analysed with a Matlab script to quantify the mean intensity in these

253 images. For each sample, the average of the mean intensity computed in the different fields of view
254 was calculated.

255 ***NanoSIMS Cellular imaging***

256 To prepare samples for NanoSIMS cellular imaging, HCT116 cell spheroids already incubated with 2mM
257 AGuIX® nanoparticles for 72h were fixed with 2% glutaraldehyde in cacodylate buffer (0.1 M, pH 7.8)
258 for 60 minutes, followed by rinsing with PBS (3 times, 5min each). Samples were then postfixed with
259 1% osmium tetroxide follow by uranyl acetate staining and gradually dehydrated in ethanol (30% to
260 100%) and embedded in Epon.
261 A 0.2 µm relatively thick section was deposited onto clean Si chip and dried in air before being
262 introduced into a NanoSIMS-50 Ion microprobe (CAMECA, Gennevilliers, France) operating in scanning
263 mode [44,45]. For the present study, a tightly focused Cs^+ primary ion beam at an impact energy of 16 keV
264 was used to monitor up to five secondary ion species in parallel from the same sputtered volume: $^{12}C^-$
265 , ^{12}C, $^{14}N^-$, $^{28}Si^-$, $^{31}P^-$, as well as $^{35}Cl^-$. The primary beam steps over the surface of the sample to create
266 images for these selected ion species. The primary beam intensity was 3 pA with a typical probe size
267 of ≈200 nm. The raster size was 60 µm with an image definition of 512×512 pixels. The acquisition was
268 carried out in multiframe mode with a dwell time of 0.5 ms per pixel and 220 frames were recorded.
269 The Image processing was performed using the "ImageJ" software [46]. Successive image frames were
270 properly aligned using TOMOJ plugin [47] with ^{12}C and $^{14}N^-$ images as reference to correct the slight image
271 field shift during the 8 hours signal accumulation, before a summed image was obtained for each ion
272 species.
273

Results and Discussion

A hydrogel-based microsystem was developed to generate uniform-sized multicellular tumour spheroids (**Fig. 1**). The design of these microwells was meant to meet the following goals: 1) making homogenous and uniform cell spheroids 2) increase the throughput in drug screening 3) be compatible with *in-situ* treatment, immunostaining and image acquisition as well as *ex-situ* characterization techniques. First, a silicon wafer mould is designed and made using classical photolithography technique (**Fig. 1A**). From this silicon wafer mould, counter moulds in Polydimethylsiloxane (PDMS) are prepared (**Fig. 1B**), which can be used several times to replicate microwells with agarose hydrogel. To prepare agarose microwells, 2% ultra-pure agarose solution is poured on PDMS moulds (**Fig. 1C**) and after gelation, they can be placed on APTS functionalized cover slips (**Fig. 1D**) or directly transferred to any classical multi-well plate (**Fig. 1E**).

This method enables us to generate hundreds of homogenous spheroids per micro-system in each well of a multi-well plate (**Fig. 1E, F**). Thanks to the hydrogel nature of the microwells, many experimental steps including rinsing, changing medium, spheroid fixation and immunostaining could be implemented in the same multi-wells plate, with no manipulation of spheroids, which results in the treatment and labelling of several spheroids simultaneously (**Fig. 1G**). The advantage of the agarose microwells is the efficient transfer of medium and solutions through it. The exchange rate has been quantified by following-up the removal of a FITC dye from the agarose microwells via time-lapse image acquisition using confocal microscopy (**Fig.SI.2**). All curves are exponentially decreasing with a characteristic time of 25 minutes (23-27 min depending on the depth of the focal plane). After the first two hours, there is a 75±5% reduction in the initial mean intensity in the microsystem, reaching a plateau at 25±5 % depending on the depth of the focal plane.

Of note, the compatibility of our hydrogel-based microsystem with cover-slips enables *in-situ* quantification of nanoparticle penetration and their 3D distribution within spheroids with high-resolution optical microscopy such as confocal fluorescence microscopy (**Fig. 1H**). All spheroids are within the same focal plane, giving access to easy parallelization of 3D spheroids imaging (**Fig. 1I**). This is an important aspect compared to already proposed hydrogel microwells, where spheroids need to be transferred to a dedicated microscopic-plate for high-resolution 3D imaging [27,48–50] . Such transfer first increases the complexity in terms of handling and imaging, and second may induces fusion between spheroids, or deformation of spheroids, which in turn may introduce biases in the analysis. Our original and simple process (Biocompatible hydrogel microwell plate, under patent)[51] bridge an important gap for in-depth optical spheroid analysis.

Moreover, these microwells are compatible with time-lapse optical microscopy, facilitating follow-up of spheroids growth for several days (**Fig. SI.3, movie 1**). The system enables to produce very homogenous spheroids (**Fig. SI.4**), which give access to the heterogeneity of cell response, with no bias induced by size heterogeneity. In our study, nanoparticles penetration is mainly evaluated using fluorescent intensity obtained from 3D confocal image acquisition. Taking advantage of the large statistics we can get with our microsystems, we assessed the minimum number of spheroids required to get reliable results (**Fig. SI.5**). A minimum of N=30 spheroids is recommended to get reliable results at an imaging depth corresponding to the first quarter of the spheroids (0-50 µm from the periphery). This number rises up to N=70 spheroids for an accurate analysis close to the equatorial plane.

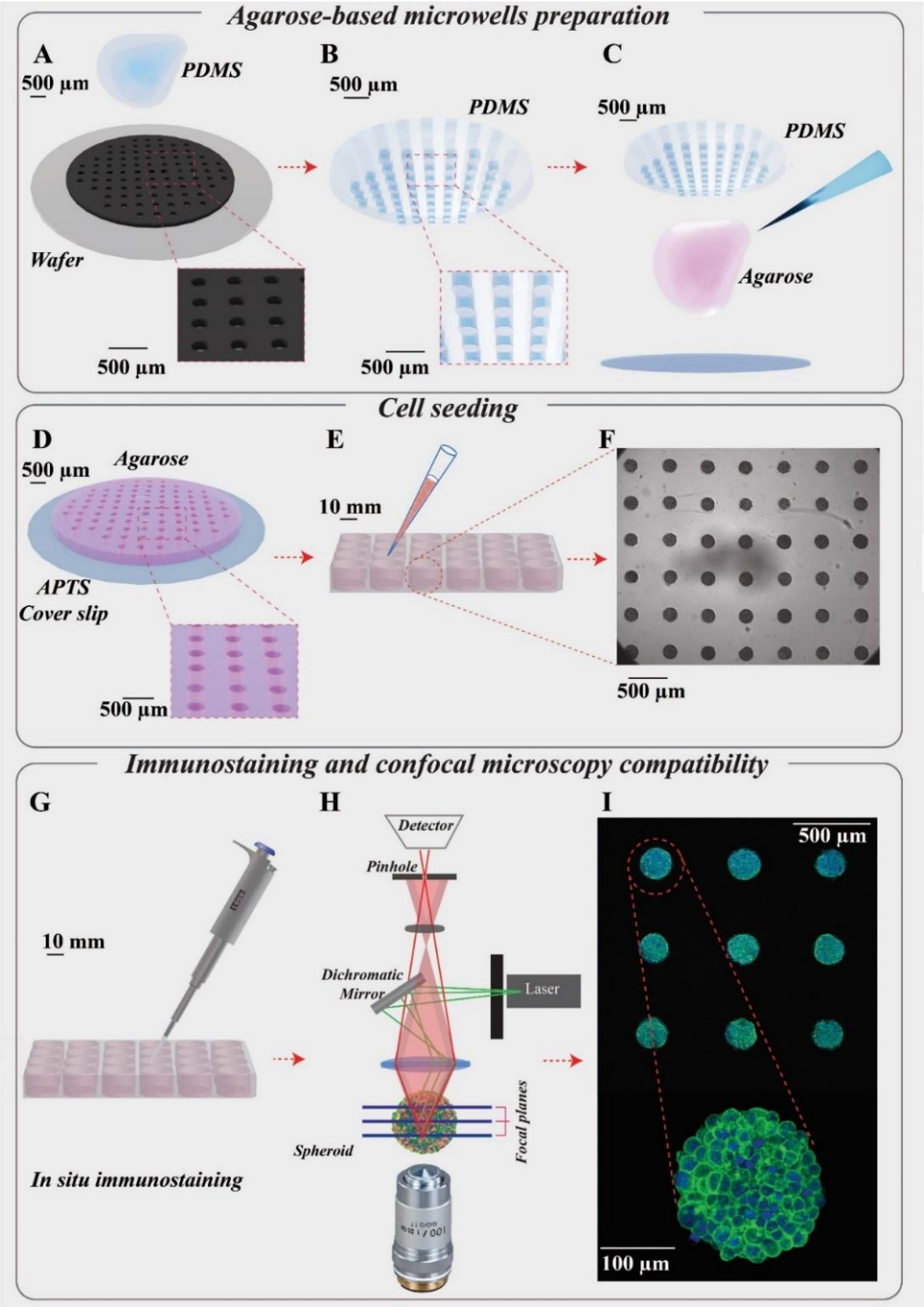

Figure.1. Presentation of the hydrogel-based microsystems for spheroids growth and follow-up (A) *silicon wafer mould made by photolithography.* ***(B)*** *PDMS replica mould made from the silicon wafer mould.* ***(C)*** *Moulding of agarose using PDMS replica moulds on a cover slip functionalized by APTS to make the agarose microsystem adhesive on the cover slip.* ***(D)*** *Cylindrical agarose microwells with diameter and height of 200 µm for each microwell.* ***(E)*** *cell seeding using agarose microsystem in a 24-wells plate for preparation of spheroids.* ***(F)*** *Optical microscopy images of several homogenous HCT116 cell spheroids made in agarose microsystem (5X magnification) at day 6.* ***(G)*** *In situ immunostaining of spheroids in microwells in a 24-wells plate.* ***(H)*** *Diagram of confocal fluorescence microscopy.* ***(I)*** *Maximal Image Projection (MIP) of confocal fluorescence images of spheroids in agarose microsystem labelled for actin (green) and nuclei (blue) (10X magnification) and an enlarged MIP of one of the spheroids (20X magnification).*

327 ***Quantification of cellular uptake of AGuIX®-Cy5 nanoparticles in 2D and 3D***
328 As a proof-of-concept of the relevance of our new hydrogel-based microsystem, the penetration and
329 distribution of AGuIX®-Cy5.5 nanoparticles within spheroids was investigated using the classical
330 colorectal cancer cell lines HCT116. In a previous study, it has been proven that localization of Gd-
331 based nanoparticles tagged with cyanine 5.5 is the same as label-free nanoparticles in U87 cells [52].
332 After 48 h of growth within 200-µm agarose microwells, spheroids were incubated with three different
333 concentrations of AGuIX®, 0,8, 1,5 and 2 mM in gadolinium, selected according to previous studies
334 performed in 2D cell culture [53]. In **Fig. 2A**. fluorescence images display the distribution of AGuIX®-Cy5.5
335 nanoparticles in spheroids after 24 h incubation with the three different concentrations at different
336 depths. These images show qualitatively that the amount of nanoparticles clusters in spheroids directly
337 increases with increase in initial concentration of AGuIX®-Cy5.5 nanoparticles. For 0.8 mM, very few
338 nanoparticle clusters could be observed, while the number of clusters increased in 1,5 and 2 mM
339 concentrations. For 2 mM concentration, nanoparticles are detected within the deeper layers of
340 spheroids. Taking the spherical geometry of the sample into account to quantify images of spheroids,
341 the mean intensity is calculated by averaging intensity along theta and phi angles in direction of the
342 radius. The *in-situ* fluorescence analysis of **Fig. 2B** enables to decipher the relative differences in
343 nanoparticles penetration in the range of concentration analysed. Consistent with the fluorescent
344 images in **Fig. 2A**, the mean intensity increases as the incubation concentration increases. From the
345 outermost layer to the centre of the spheroids, the mean intensity decreases differently depending on
346 the concentration (from 34±8% to 28±14% for 0.8 mM, from 68±8% to 46±15% for 1.5 mM and from
347 66±5% to 60±24% for 2 mM). For the largest concentration (2 mM), deep penetration is possible, while
348 the penetration decreases exponentially with the depth for 1.5 mM, with a characteristic length of
349 44±2 µm. Such difference could be attributed to the higher number of nanoparticles reaching the
350 centre of the spheroids for an incubation with 2 mM Gd. The relative independence of fluorescence
351 intensity with depth for the lowest concentration (0.8 mM), could be attributed to a level close to
352 noise, with no real penetration of nanoparticles nor in the periphery, neither in the centre of the
353 spheroids.
354 Deep penetration of small nanoparticles within deep interstitial space have already been reported *in-*
355 *vivo* [54]. The *in-vitro* platform described in this study enables to assess such penetration and it will be a
356 valuable tool to relate such penetration with therapeutic efficacy in future studies.
357 To make a direct comparison with cellular uptake in 2D cell culture, monolayers of HCT116 cells were
358 incubated with the same concentration of AGuIX®-Cy5.5 nanoparticles (**Fig. 2C**). As expected, the
359 number of AGuIX®-Cy5.5 clusters raised as the initial concentration increased and the quantification of
360 fluorescence images of cell monolayers based on the mean intensity of AGuIX®-Cy5.5 confirms that the
361 uptake of nanoparticles increases with the concentration of AGuIX®-Cy5.5 in the incubation medium
362 (**Fig. 2D** from 14.0 ±0.3 % for 0.8 mM, 25.8 ± 1.8 % for 1.5 mM to 70.8 ± 4.4 % for 2 mM). This mean
363 intensity evolution is hence different from the one obtained in 3D in the periphery. However, as a true
364 quantitative comparison is not possible using fluorescent analysis, ICP-MS technique was performed
365 in parallel to get a quantitative analysis of Gadolinium content within cells for both 2D and 3D models
366 (**Fig. 2E**). While the average nanoparticles uptake per cell in 2D and 3D are similar for 0.8 mM
367 ((0.580±0.006).10^{-14} ppb/µm^3 in 2D versus (0.59±0.05).10^{-14} in 3D), the uptake is two-fold higher in 2D
368 compared to 3D for both 1.5 mM ((2.5±0.5).10^{-14} ppb/µm^3 in 2D versus (1.0±0.2).10^{-14} in 3D) and 2 mM
369 ((3.8±0.9).10^{-14} ppb/µm^3 in 2D versus (1.9±0.6).10^{-14} ppb/µm^3 in 3D).
370 One of the reasons of the reduction in effectiveness of therapeutics *in-vivo* compared to monolayer
371 cell cultures is the lack of efficient penetration and distribution of therapeutics throughout tumour

tissue [55]. This is what we also get here, with a large reduction of nanoparticles uptake in 3D compared to 2D cell-culture.

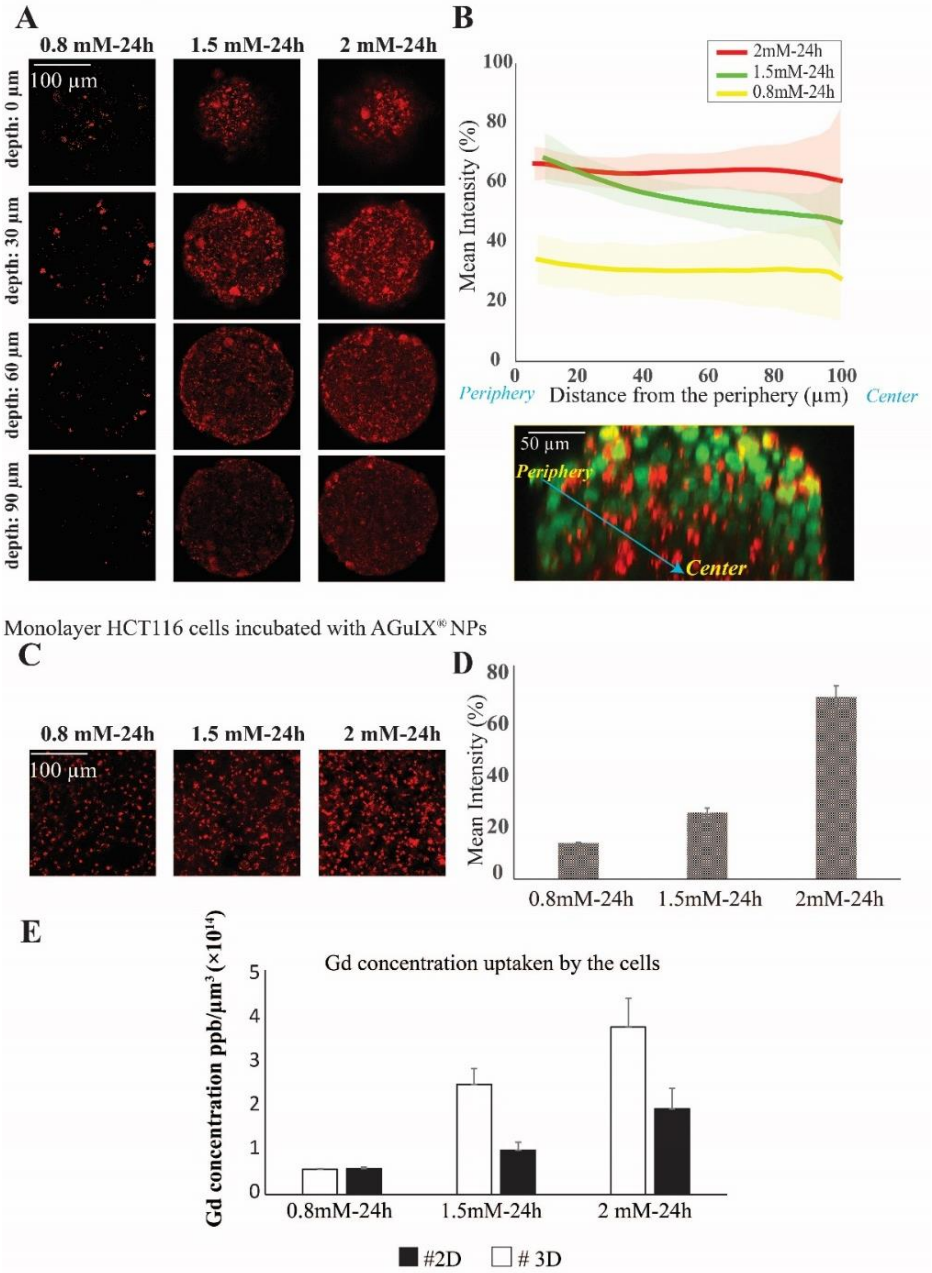

Figure.2. Quantification of penetration and cellular uptake of AGuIX®-Cy5 nanoparticles in HCT116 tumour spheroids and monolayer cell culture. ***(A)*** *Representative confocal fluorescence images of HCT116 spheroids incubated with 0.8 mM, 1.5 mM and 2 mM concentration of AGuIX® for 24 h for four different depths (0, 30 µm, 60 µm and 90 µm).* ***(B)*** *Mean intensity along with standard deviation (light colors) of AGuIX®-Cy 5.5 as a function of the distance from the spheroids periphery (see the orthogonal view in the inset, green=nuclei, red = AGuIX® -Cy5.5) for 0.8 mM (yellow, N=73), 1.5 mM (green, N=68) and 2 mM (red, N=121), three independent experiments.* ***(C)*** *Representative confocal fluorescence images of monolayer HCT116 cells exposed to AGuIX®-Cy5 nanoparticles with 0.8 mM, 1.5 mM and 2 mM.* ***(D)*** *Quantification of the mean intensity of AGuIX® NPs in maximal projection of confocal fluorescence images of monolayer cells after 24h incubation with different AGuIX® concentrations: 0.8 mM (yellow, N=40), 1,5 mM (green, N=40) and 2 mM (red, N=40), three independent experiments.* ***(E)*** *Mean and standard deviation of the concentration of Gd (ppb/µm³) uptaken by the cells after incubation with 0.8 mM, 1.5 mM and 2 mM concentration of AGuIX® for 24 h in HCT116 cell spheroids and monolayer cell culture measured with ICP-MS technique (N = 6, two independent experiments).*

388 ***Study of the Kinetics of AGuIX®-Cy5 nanoparticles transport into spheroids***

389 One of the crucial parameters in nanoscale design is the pharmacokinetics of nanoparticles and
390 understanding this aspect of cell-nanoparticles interactions has a great importance [56,57]. The kinetics
391 of penetration of AGuIX®-Cy5.5 nanoparticles within HCT116 cell spheroids grown for 48 hours were
392 assessed by analysing confocal images obtained for different incubation times (1, 24 and 72 hours), for
393 the highest concentration investigated (2 mM) (**Fig. 3A**). After 1 hour incubation, the AGuIX®-Cy5.5
394 nanoparticles are mostly residing in the peripheral layer of the spheroids, especially in the extracellular
395 space. After 24 h, clusters of nanoparticles are found throughout the spheroids. At 72 h, the number
396 of clusters are increasing for all depth, up to the equatorial plane (100 µm).

397 The average intensity is exhibiting different evolution with the distance from the periphery, depending
398 on the incubation time (**Fig. 3B**). At the periphery, the average intensity is lower for 1 hour incubation
399 (52.2±1.3%) than for 24 h and 72 h that exhibit similar values (68±1% and 65.8±0.7%, respectively).
400 When we move to the centre of the spheroids, the mean intensity is slightly decreasing for 1 h and 24h
401 incubation (from 52.2±1.3% down to 38.7±2.7% for 1h, from 68±1% down to 59.5±1.9 % for 24 h).
402 Accordingly, in 1 h incubation the mean intensity is less than 24 h and 72 h samples in all regions of
403 the spheroids. Surprisingly, for 72 h, the average intensity exhibits a non-monotonous evolution with
404 the distance from the periphery, with an intensity larger at the centre than at the periphery (66±5% vs
405 73.8 ±8.5% at a depth of 60 µm from the periphery). This may be the results of increased number of
406 clusters found for intermediate layers after 72h incubation time.

407

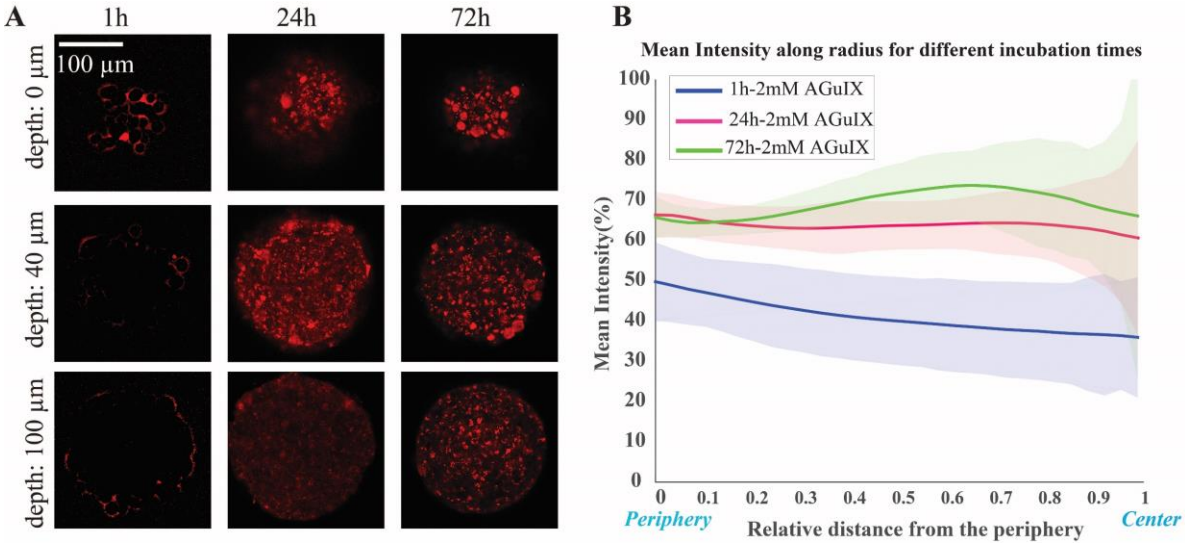

408

409 **Figure.3. Kinetics of penetration of AGuIX®-Cy5 nanoparticles in HCT116 cell spheroids**.

410 ***(A)*** *Representative confocal fluorescence images of HCT116 grown for 48h, exposed to 2mM concentration of*
411 *AGuIX®-Cy5 nanoparticles for 1 h, 24 h and 72 h.* ***(B)*** *Mean intensity along with standard deviation (light colours)*
412 *as a function of relative distance from the periphery for 1h (blue, N=50), 24h (magenta, N=121) and 72h (green,*
413 *N=63), three independent experiments.*

414

415 To follow the distribution and the transport of nanoparticles within spheroids, an experiment was
416 designed to assess changes in AGuIX®-Cy5.5 nanoparticles distribution before and after rinsing steps
417 (**Fig. 4**). In this experiment, after cell seeding (**Fig. 4 step I**), at day 2, the formed HCT116 spheroids
418 were incubated with 2mM AGuIX® solution for 72 h (**Fig. 4, step II**). Spheroids were then imaged in
419 incubation medium (**Fig. 4 step III**) and after three washing steps, 15 min each (**Fig. 4 step IV**).
420 Spheroids were kept in the incubator for additional 24 h and then imaged before (**Fig. 4 step V)** and
421 after (**Fig. 4 step VI**). another washing procedure. In the confocal fluorescence images obtained for live
422 spheroids, we can see that the AGuIX® -Cy5.5 nanoparticles fluorescence signals of the surrounding
423 background is decreasing gradually with the different washing steps for all depth (**Fig. 4A-D**). This is
424 confirmed by the quantification of the mean intensity along the spheroid radius (**Fig. 4E**): while the
425 mean intensity before washing (red curve) at the periphery is around 92±10%, it is decreasing to
426 59±10% at 55 µm distance from the periphery. After the first washing step (yellow curve), the mean
427 intensity at the periphery reduced to 66±6%, and reached a similar intensity level than to the one
428 before washing at 55 µm distance from the periphery (58±4%). Further washing steps further reduced
429 the mean intensity at the periphery (64±14% and 54±14% before and after the second washing step),
430 while the mean intensity obtained for deeper layers exhibit similar levels. The last curve corresponding
431 to imaging after the second washing (blue curve), displays a steady value (~54%) of mean intensity
432 close to the mean intensity obtained at 55 µm distance from the periphery of spheroids for all washing
433 steps. This mean intensity should correspond to the signal coming from nanoparticles that are
434 internalized by the cells, as all nanoparticles residing in the extracellular space have been washed
435 away.
436

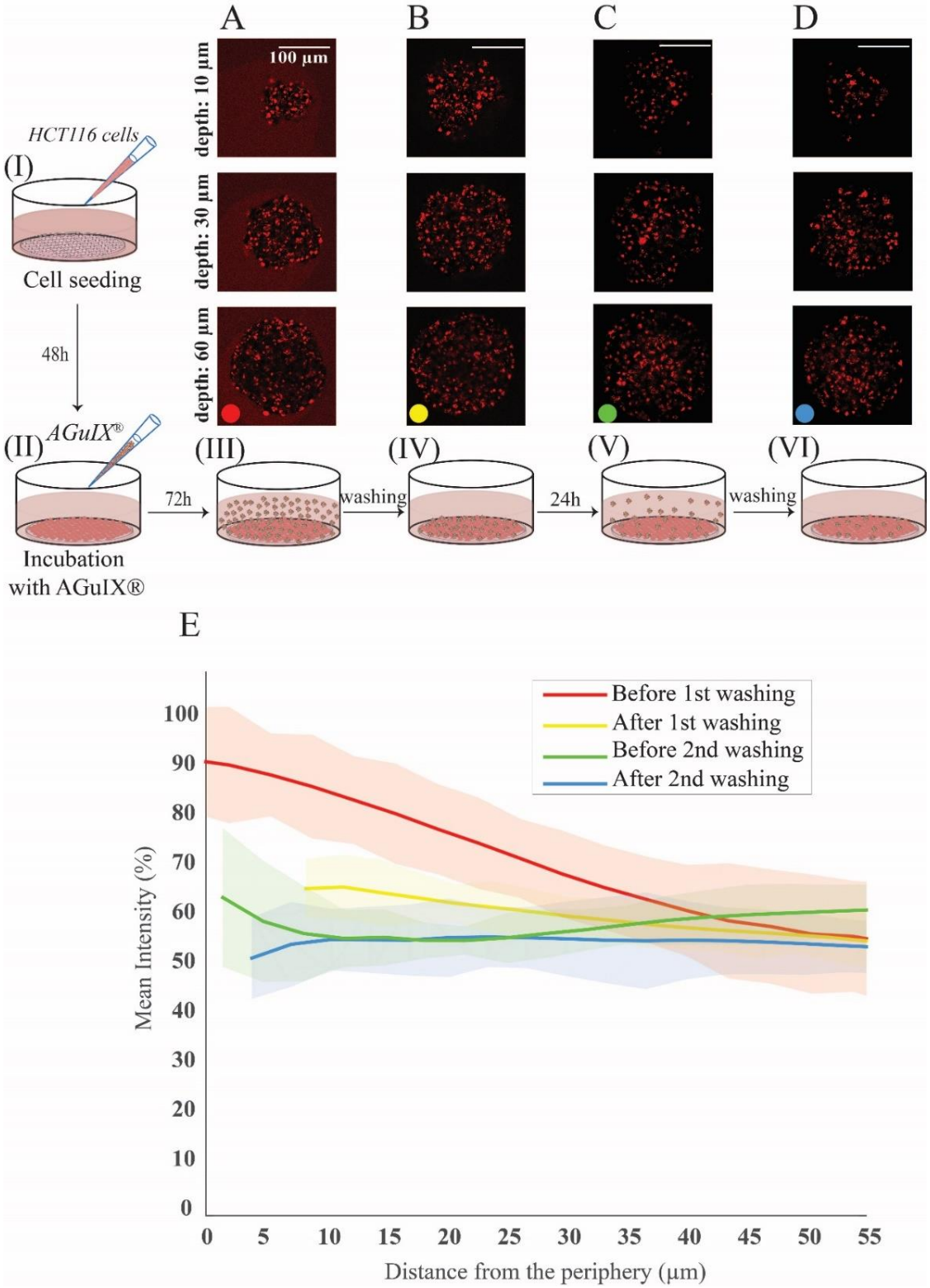

Figure.4. Dynamic analysis of AGuIX®-Cy5 nanoparticles transport and localization within spheroids. *HCT116 cells spheroids were prepared using agarose microsystem **(step I).** After 48 h growth, they were exposed to 2 mM AGuIX®-Cy5 solution for 72 h **(step II)**. **(A)** spheroids were imaged in the incubation medium **(step III)**. **(B)** Spheroids were then rinsed with fresh medium three times for 15 minutes each and were imaged again **(step IV).** **(C)** Spheroids were allowed to grow for an additional 24h (in an incubator at 37°C and 5% CO_2), and were imaged directly **(step V). (D)** Spheroids were rinsed again with fresh medium three times, 15 min each **(step VI)**. **(E)** Quantification of AGuIX®-Cy5 nanoparticles mean intensity along the distance from the periphery (N=25). Bold Lines represent the mean intensity, averaged for all spheroids. Light colors represent the Standard Deviation.*

446 ### *Localization of nanoparticles in spheroids using their chemical signature*

447 Due to the limit of standard confocal optical microscopy resolution (200 nm in the best imaging
448 conditions), only clusters of nanoparticles can be detected. In addition, we can not rule out that the
449 distribution of the fluorophore do not truly represent the distribution of the nanoparticles themselves.
450 To confirm the presence of nanoparticles, **nanoscale Secondary Ion Mass Spectrometry** (**nanoSIMS**)
451 was performed on spheroids sections (**Fig. 5**). This analytical technique allows the acquisition of
452 elemental composition maps with a spatial resolution down to 50 nm. The images of $^{12}C^-$ (see **Fig.SI.7**)
453 and $^{35}Cl^-$ (data not shown) indicates the condition of the analyzed area. Any damage, even tiny holes,
454 would appear with high contrast in signal, such signal is not observed here indicating that the section
455 is not damaged. This validates that the signal measured was originated from the sample and not from
456 the subjacent pure silicon substrate. The image of ^{12}C and $^{14}N^-$ shows the histological aspect of the cell
457 (data not shown) while the one of $^{31}P^-$ (**Fig. 5A**) highlights the cell nucleus. Since AGuIX NPs are mainly
458 made of Si, the images of $^{28}Si^-$ allows the observation of the chemical signature of the NPs (**Fig. 5B**).
459 Thereby, the NPs are found unequivocally inside the spheroid, exclusively in the cytoplasm of the cells.
460 Of note, again our microsystems enable an easy sample preparation, as all spheroids are within the
461 same sectioning plane.

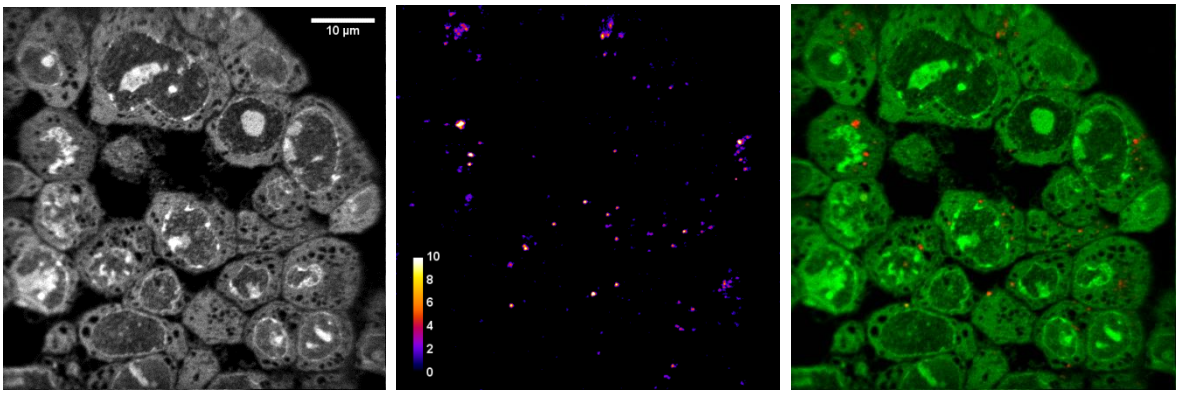

462
463 A B C
464

465 **Figure 5. Localization of the nanoparticles in spheroids using NanoSIMS.**
466 *NanoSIMS images of HCT116 cells loaded with AGuIX-Cy5 nanoparticles.* ***(A)*** *corresponds to the signal of* $^{31}P^-$
467 *showing the cell structure.* ***(B)*** *highlights the signal of* $^{28}Si^-$ *representing the intracellular location of AGuIX NPs.*
468 ***(C)*** *Merged image of* $^{28}Si^-$ *and* $^{31}P^-$*. Scale bar: 10 µm.*

469 ### *Assessment of nanoparticles localization within cells in 2D and 3D with immunostaining.*

470 Thanks to the full compatibility of our microsystems with *in situ* immunostaining, it is possible to assess
471 the localization of nanoparticles in 2D cells (**Fig. 6**) and multicellular tumour spheroids (**Fig. 7**), using
472 confocal fluorescence microscopy.

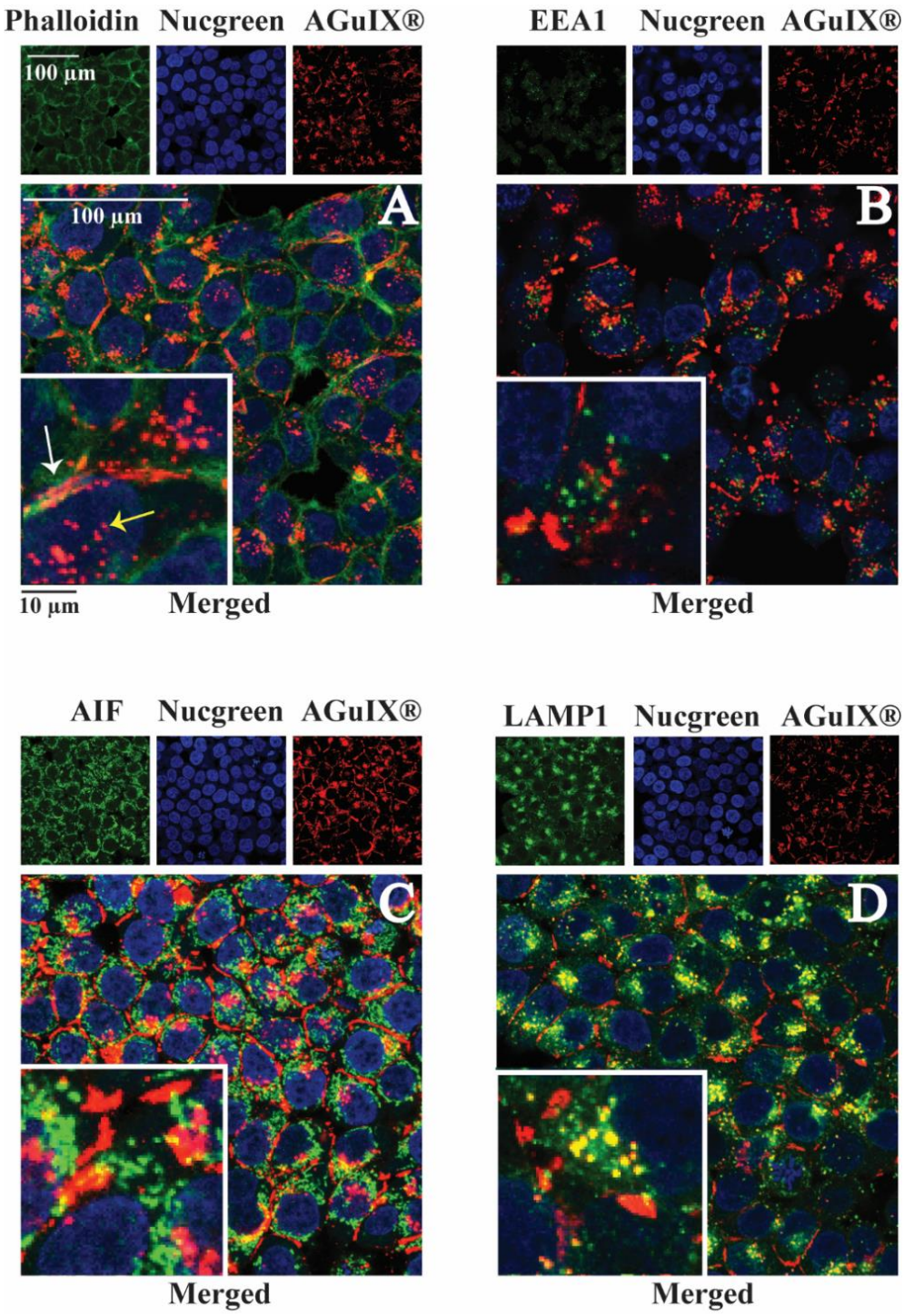

Figure 6. **Localization of the nanoparticles *in 2D monolayers.***

Fluorescence images of HCT116 cells incubated with AGuIX-Cy5 nanoparticles (2mM, 24h) and immunostained with antibodies to find colocalization of nanoparticles inside cells. In all images red channel and blue channel represent AGuIX® nanoparticles and cell nuclei respectively. ***(A)*** *Green channel depicts phalloidin, a marker of actin in cells, which demonstrates nanoparticles localizing both inside cells (yellow arrow) and in the space between cells (white arrow).* ***(B)*** *Green channel shows early endosome in the cells, with no colocalization with AGuIX®-Cy5 nanoparticles.* ***(C)*** *mitochondria in the cells are labelled in Green, with no colocalization with AGuIX®-Cy5 nanoparticles.* ***(D)*** *Green channel demonstrates lysosome and yellow colour is a representative of colocalization of nanoparticles in red and lysosome in green. White scale bar, 100 µm and black scale bar, 10 µm.*

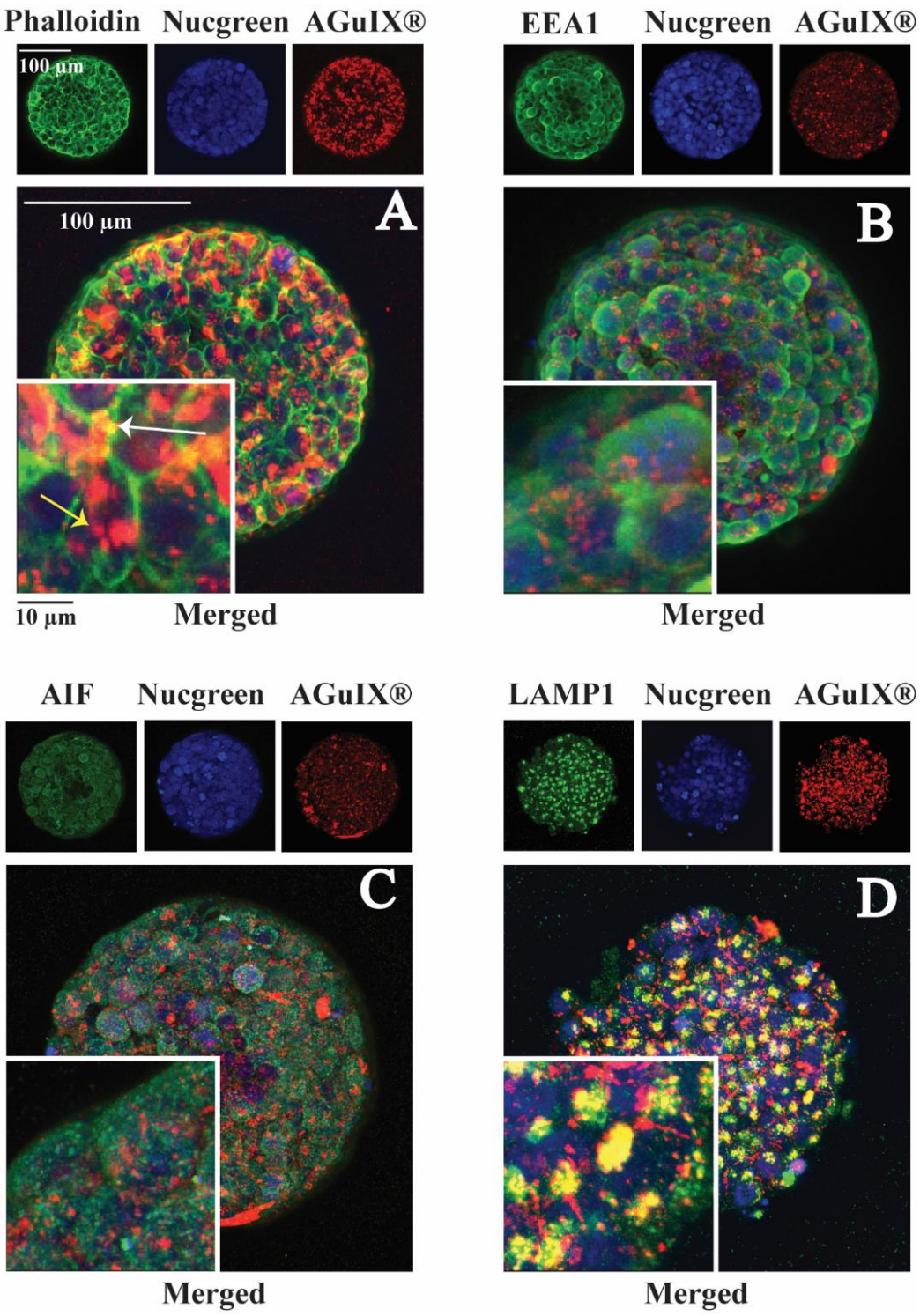

Figure 7. Localization of the nanoparticles within spheroids.

Fluorescence images of HCT116 cells spheroids incubated with AGuIX®-Cy5 nanoparticles (2mM, 24h) and immunostained with antibodies to find colocalization of nanoparticles inside cells. In all images red blue channels represent AGuIX®-Cy5 nanoparticles and cell nuclei respectively. ***(A)*** *Green channel depicts phalloidin, a marker of actin in cells, which demonstrates nanoparticles are localizing inside both cells (yellow arrow) and the extracellular space of spheroid (white arrow).* ***(B)*** *EEA1 antibody in green channel shows early endosome in the cells; with no colocalization with nanoparticles.* ***(C)*** *AIF antibody labelled mitochondria in cells is shown in Green, with no colocalization with AGuIX®-Cy5 nanoparticles.* ***(D)*** *LAMP1 antibody in green channel, staining lysosomes in green. Yellow colour represents the colocalization of nanoparticles in red and lysosomes in green. White scale bar, 100 µm and black scale bar, 10 µm.*

494 Labelling of cell organelles confirmed that nanoparticles are present in both extracellular and
495 intracellular space in 2D cells (**Fig. 6A**) and in 3D spheroids (**Fig. 7A**). No colocalization of AGuIX®-Cy5
496 with early endosomes (**Fig. 6B in 2D and Fig. 7B in 3D**) or mitochondria (**Fig. 6C in 2D and Fig. 7C in**
497 **3D**) is evidenced by immunostaining, while a clear colocalization with lysosome is observed in both 2D
498 (**Fig. 6D)** and 3D conditions (**Fig. 7D**). Noteworthy, this colocalization is not total and some
499 nanoparticles are still residing in between cells. These findings are associated with previous studies
500 showing localization of nanoparticles in endocytic pathway and in lysosomes [38,52]. Moreover, it
501 implicates that localization of these nanoparticles is the same for monolayer cells and cells in HCT116
502 multicellular spheroids.
503 As highlighted with the overall mean intensity decrease with washing procedure for the peripheral
504 layers of the spheroids (**Fig. 4**), the extracellular nanoparticles are efficiently washed away after long
505 washing procedure (**Fig. 8A**, no extracellular nanoparticles detected with immunostaining). Similar to
506 results obtained after 72h incubation, co-localization with lysosomes is still the preferable localization
507 of nanoparticles after washing procedure (**Fig. 8C**). A clear difference in the distribution is however
508 evidenced, with co-localization found mostly in inner layers (**Fig. 8C**), suggesting nanoparticles
509 trafficking after such washing procedure. More surprisingly, some co-localization with mitochondria is
510 evidenced (**Fig. 8B),** that could be attributed to intracellular trafficking of nanoparticles over time.

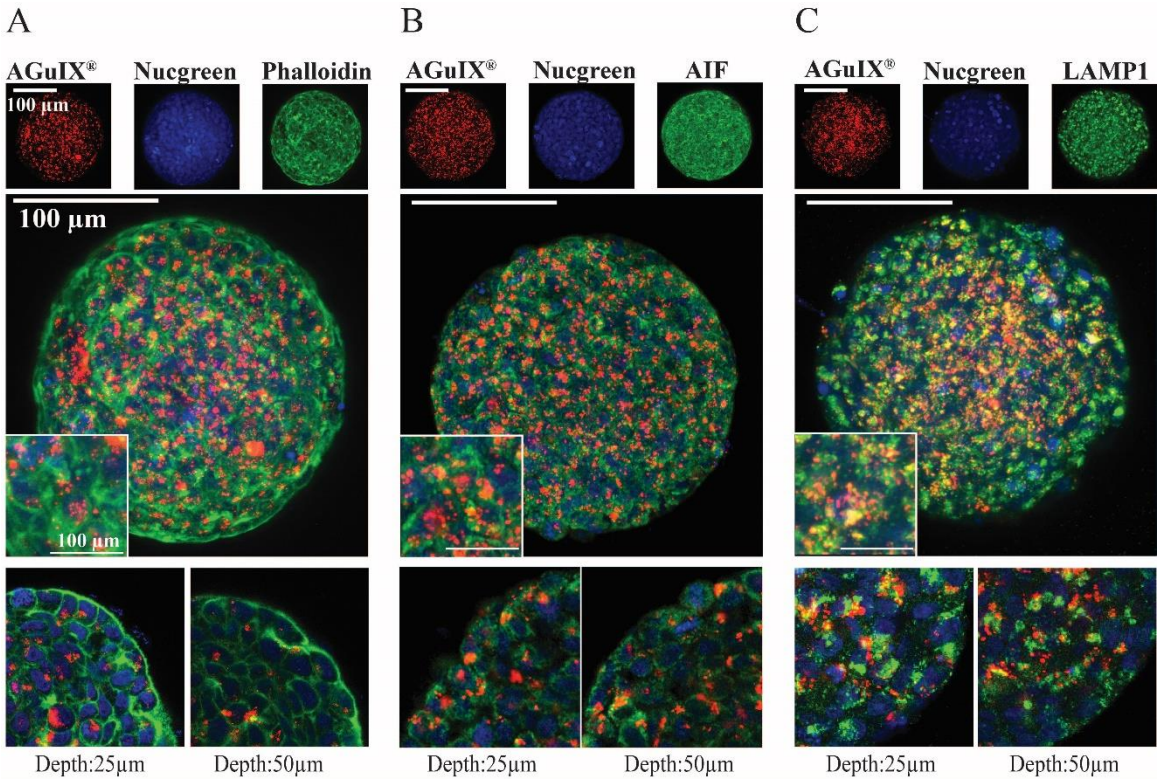

511
512 ***Figure 8. Localisation of Aguix-Cy5-nanoparticles after an extensive washing procedure.***
513 *Confocal fluorescence images of HCT116 cells incubated with AGuIX®-Cy5 nanoparticles for 72h with 2mM AGuIX®*
514 *solution, washed according the procedure mentioned in Figure 4, then fixed and immunostained with antibodies*
515 *to find colocalization of nanoparticles in spheroids, in all images red channel and blue channel represent AGuIX®*
516 *nanoparticles and cell nuclei, respectively.* ***(A)*** *Green channel depicts phalloidin, a marker of actin in the cells,*
517 *which demonstrates nanoparticles that are mostly inside cells after washing procedure.* ***(B)*** *AIF antibody labelled*
518 *mitochondria in cells is shown in Green, yellow colour in merged image indicate possible translocation of AGuIX®*
519 *nanoparticles inside cells after washing procedure and colocalization in mitochondria.* ***(C)*** *LAMP1 antibody in*
520 *green channel demonstrates lysosome and yellow colour in this image is a representative of colocalization of*
521 *nanoparticles in red and lysosome in green.*

522 ## Conclusion and outlooks

523 We show in this study a simple agarose-based microsystem to quantitatively assess nanoparticles
524 penetration within 3D-cell culture model. The reproducibility of the spheroid size obtained with such
525 procedure dispenses the use of sophisticated automatic procedure to choose and pick the appropriate
526 spheroids. Of note, our microsystems can be manufactured on conventional multi-well plates. It is
527 hence fully compatible with available multi-well automated strategies[58]. In the present study, the
528 proof-of-concept was made using spheroids made with the classical colorectal cell line HCT-116.
529 Nevertheless, our approach is fully compatible with primary cells from patients that could be grown as
530 organoids [59] in our microsystems, combining full optical microscopy compatibility, size and shape
531 reproducibility, and large statistics. Combined with optical and digital clearing [60], our approach opens
532 up the possibility to resolve tumour heterogeneity, at the single cell-level, in a physiological context.
533 In the present study, the standard agarose used for the preparation of the microsystems provides a
534 cell-repellent surface, with a stiffness in the 150 kPa range [61,62]. In future studies, the mechanical
535 properties of the agarose gels can be adjusted using different concentrations and type of agarose.
536 Elastic hydrogels as soft as 1 kPa can be obtained using low concentration of ultra-low agarose [61],
537 matching the physiological range of stiffness. It now calls for dedicated studies to assess how
538 nanoparticles penetration and therapeutic efficiency is affected by the size of the 3D-cell assembly,
539 the presence of an extracellular matrix of different stiffness and composition, and the presence of
540 associated tumour cells [63].

541 ## Acknowledgments

542 This work was supported by the “Institut Universitaire de France” (IUF). We thank L. Fuoco for their
543 help in the early development of this project, R. Fulcrand for his support in photolithography, M.G.
544 Blanchin for her help in spheroid preparation protocols for Electron Microscopy, as well as the CTµ
545 platform (Centre Technologique des Microstructures) for resin embending of spheroids.

546

547 ## Supplementary Figures

548 ### *Figure SI 1: Quantification of photon penetration within spheroids*

549 In optical imaging of thick three-dimensional biological samples, light scattering due to mismatch of
550 refractive index between cellular components limits imaging of deep layers in these samples [64]. To deal
551 with this issue and to evaluate clarification techniques on enhancement of confocal microscopy of
552 multicellular tumour spheroids, HCT116 spheroids were prepared via agarose microwells and fixed 72h
553 after cell seeding. Nuclei were then stained using Nucgreen™ -Dead 488. Two of the samples were
554 incubated in RapiClear or 80%/20% glycerol/PBS solution overnight and the third sample was kept in
555 PBS. All samples were then mounted in iSpacers (2x0.5 mm) with fresh clarification solutions or fresh
556 PBS for control sample. Ten spheroids from each sample were imaged. A qualitative analysis of the
557 images (**Fig. SI 1A**) shows that nuclei fluorescence signal is detected much deeper for clarified
558 spheroids compared to unclarified ones. The orthogonal views of spheroids confirm this (**Fig. SI 1B**).
559 These images were analysed using a routine prepared in Matlab to measure the average fluorescence
560 intensity along the spheroids radius (**Fig. SI 1C**). The mean Intensity of spheroids clarified with glycerol
561 (Green curve) shows the highest mean intensity for all regions in spheroids compared to the two other
562 samples. While the mean intensity of RapiClear-clarified spheroids (Red curve) is lower than glycerol-
563 clarified spheroids in all regions of the spheroids, the intensity decay is similar for both clarified
564 solutions. The 80% glycerol solution was hence selected as the standard clarification technique for all
565 this study.

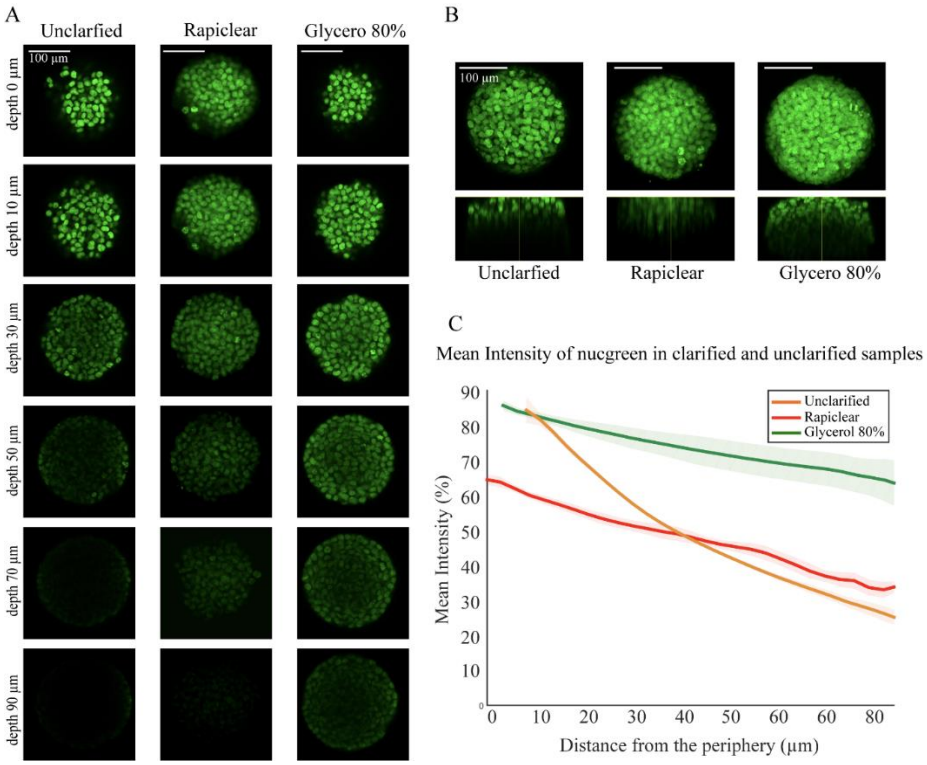

566

567 ***Figure SI 1. Influence of clarification technique on image acquisition and fluorescence signals***

568 ***(A)*** *confocal fluorescence images of HCT116 cell spheroids labelled with nucgreen in different depth for*
569 *unclarified, clarified with Rapiclear and clarified with 80%/20% Glycerol/PBS respectively.* ***(B)*** *Maximal Image*
570 *Projection (MIP) and xz images of clarified and unclarified spheroids.* ***(C)*** *Mean intensity of clarified (green,*
571 *glycerol-clarification, red, rapiclear-clarification) and unclarified (orange curve) spheroids as a function of the*
572 *distance from the periphery. Error bars represent standard errors of the Mean (N=10 spheroids for each*
573 *condition).*

574

575 ***Figure SI 2: Quantification of the removal of FITC in agarose-based microwells***

576 To understand the ability of agarose gel in transporting molecules, the agarose-based microsystems
577 were incubated with a FITC solution (0.05 mM). FITC solution was then replaced with PBS and the
578 removal FITC dye was imaged with time-lapse confocal microscopy. The images of different depths of
579 agarose-based microwells were analysed using a routine prepared in Matlab to quantify the mean
580 intensity changes with the time (**Fig. SI 2**). After the first two hours, there is a 75±5% reduction in the
581 initial mean intensity in the microsystem, reaching a plateau at 25±5 % depending on the depth of the
582 focal plane.

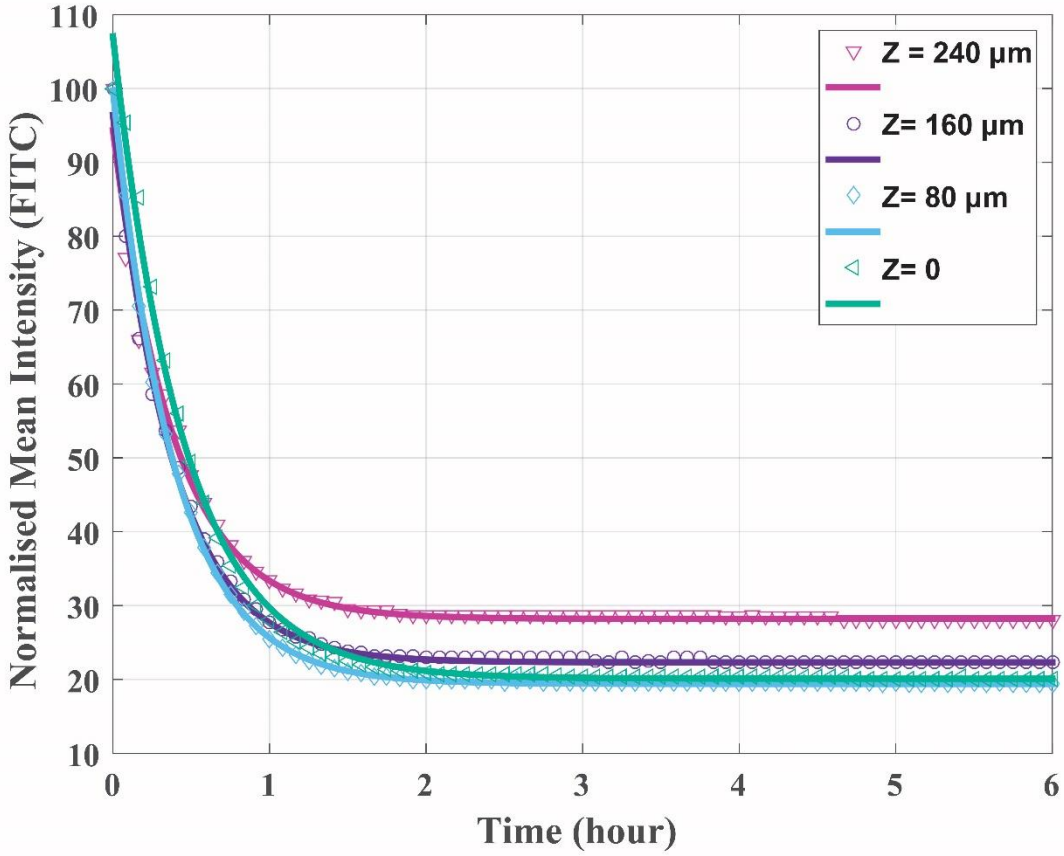

583

584 **Figure SI 2.**

585 *Reduction in fluorescence intensity of FITC dye in agarose microsystem over the time for different depth in an*
586 *agarose-based microwell (from Z=0, corresponding to the depth closest to the objective and farthest from the*
587 *solution reservoir to Z=240 µm, farthest from the objective and closest to solution reservoir). Experimental points*
588 *are plotted with different markers (Z=0, (pink triangles pointing down), Z=80 µm (blue diamonds), Z=160 µm*
589 *(purple circles), Z=240 µm (green triangles pointing left)) and the corresponding exponential fit are plotted in bold*
590 *lines [fitting model a*exp(-time/T)+b].*

591

592 ***Figure SI 3. Time-lapse follow-up of spheroid growth***

593 To understand the influence of AGuIX® nanoparticles on the cell proliferation and growth rate of
594 HCT116 cell spheroids, cells were seeded in agarose-based microwells and after 48h, they were
595 exposed to AGuIX® nanoparticles with three different concentrations (0.8mM, 1.5mM and 2mM) and
596 control sample. The growth of spheroids has been followed by time-lapse optical microscopy during
597 three days of incubation with AGuIX® nanoparticles. These images were manually segmented using a
598 dedicated routine in Matlab. The volume of the spheroids was calculated from the computed
599 equivalent diameter and the graphs of the relative spheroids volume as a function of time were
600 plotted.

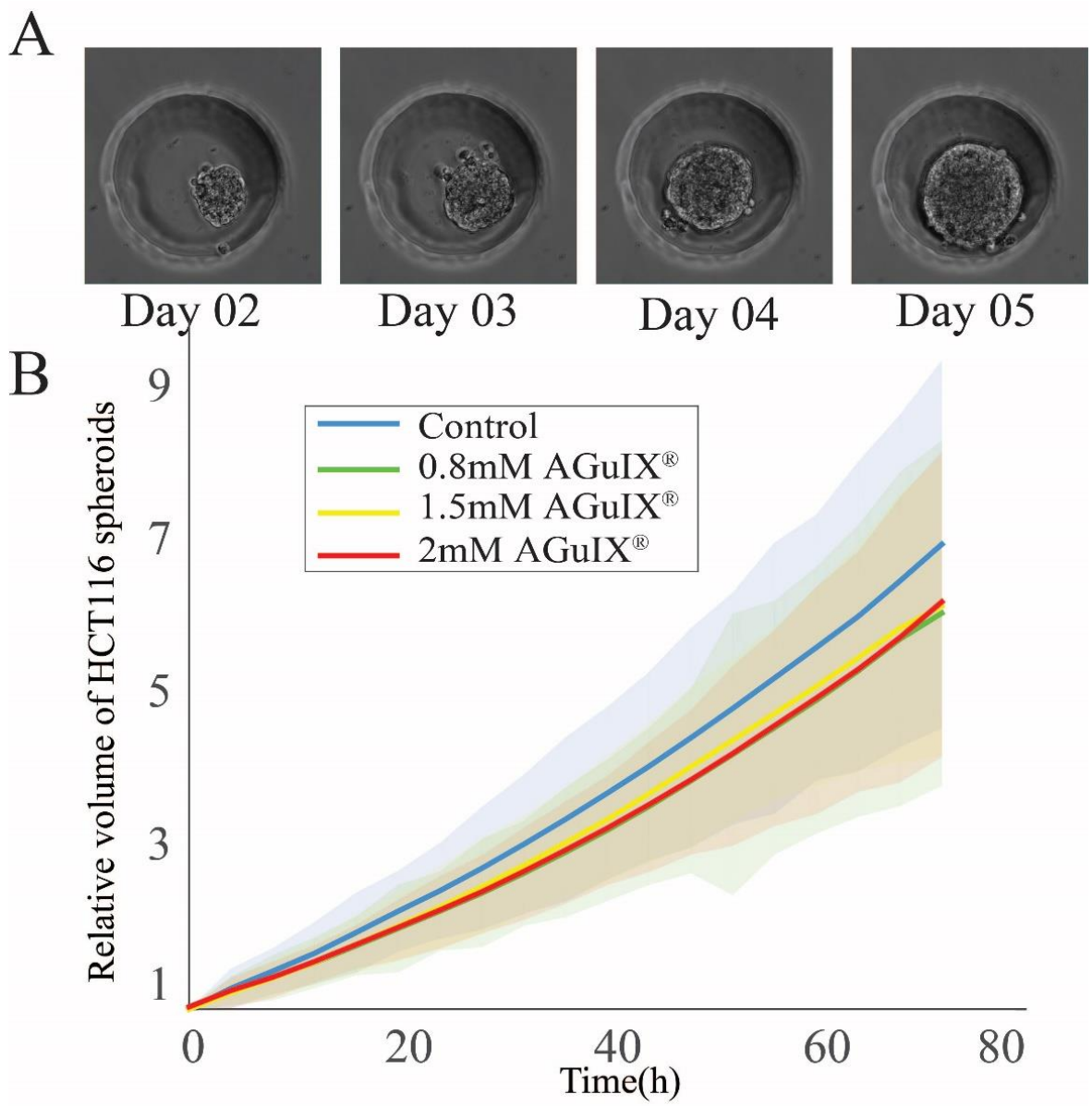

601

602 **Figure SI 3.** ***Follow-up of spheroids growth via optical time-lapse microscopy.***
603 ***(A)*** *Representative images of daily growth of HCT116 spheroids from day 2 to day 5. The well is 200 µm in*
604 *diameter.* ***(B)*** *Evolution of the relative volume of spheroids as a function of time for control sample and in the*
605 *presence of three different concentrations of AGuIX® nanoparticles. Bold lines represent the mean values, and*
606 *light area represents the standard deviation for each condition (control –blue-, 0.8mM –green-, 1.5mM –yellow-*
607 *, 2mM –red-).*

608

609 ***Figure SI 4. Characterization of spheroids size distribution from Day 2 to Day 4 after cell***
610 ***seeding***
611 One advantage of using agarose-based microwells to prepare multicellular tumour spheroids is the
612 homogeneity of spheroids size. To show the homogeneity of spheroids, the equivalent diameter for
613 each spheroid was calculated during the growth follow-up **(Fig. SI 3)**. From this, the distribution of
614 spheroids diameter in day 2, day 3 and day 4 for control conditions were plotted using the
615 UnivarScatter matlab function developed by Manuel Lera Ramírez (Copyright (c) 2015) **(Fig. SI 4)**.

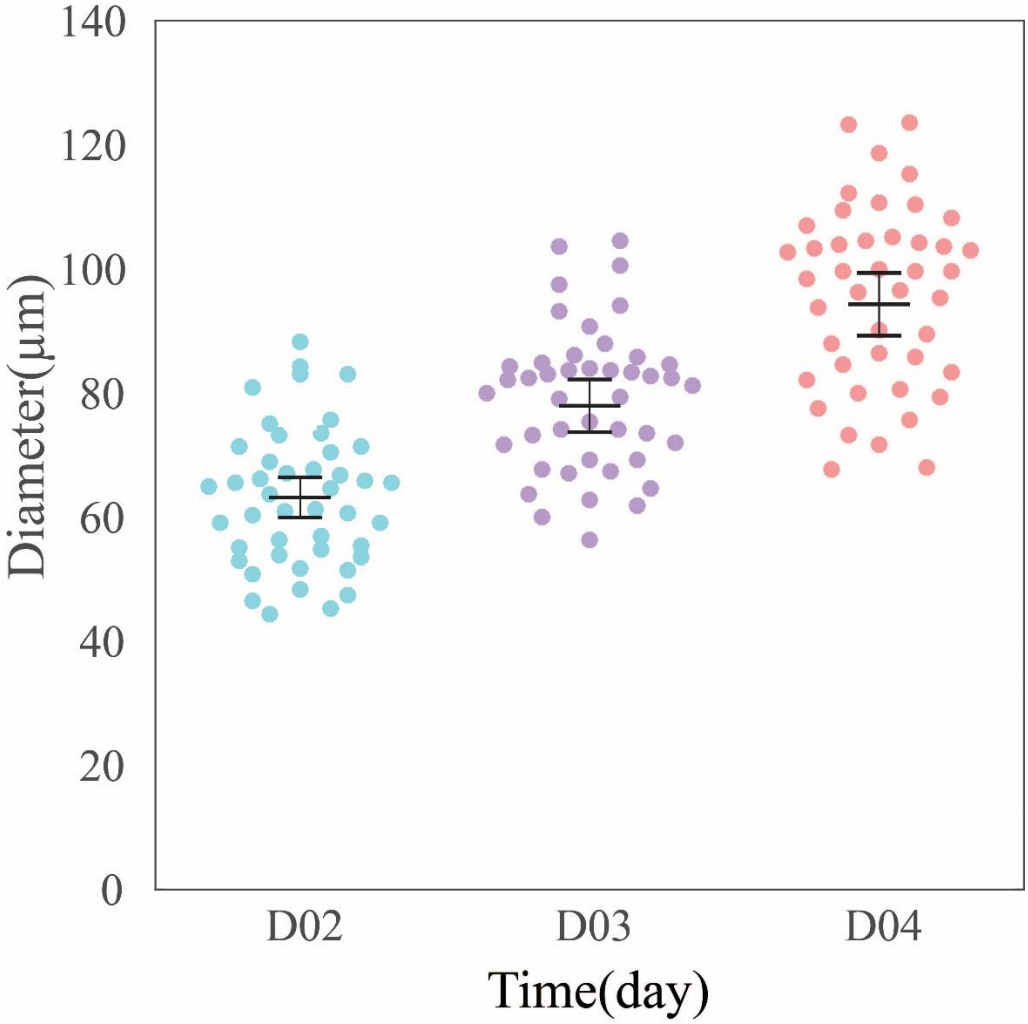

616
617 **Figure SI 4.**
618 *Distribution of HCT116 multicellular tumour spheroids at day two (blue circles), day three (purple circle) and day*
619 *four (orange circles) after cell seeding in the agarose-based microwell. Mean values and 95 % Standard Error of*
620 *the Mean are represented as large and small lines of the whiskers respectively.*
621

Figure SI 5. Importance of statistics

Due to cell heterogeneity, large statistical variances are expected, even if our process enables to generate very reproducible spheroids in terms of size. The variance on the Mean Intensity of the fluorescence signal of AGuIX®-Cy5.5 nanoparticles is analysed in **Fig.SI5**, for different distance from the periphery.

The Standard Deviation SD of the normalized Intensity of AGuIX®-Cy5.5 obtained, is calculated as a function of the number (N) of spheroids, with a random sampling of N spheroids over the 121 spheroids acquired for this experimental condition (24h incubation with 2mM AGuIX®-Cy5.5). The random sampling is repeated 10 times to simulate 10 different experiments, and the mean of the obtained SD computed. The obtained SD first increases, until reaching a plateau around N=20-40 spheroids (**Fig. SI5, Inset**). The initial rising may be attributed to the heterogeneity among spheroids. The plateau of the SD is increasing with the distance from the periphery (with a plateau at ~5% for 30 and 50 µm from the periphery, and up to ~10% for 80 µm from the periphery).

Once the plateau is reached, the standard error of the mean (SEM) and the relative standard errors (RSE=SEM/mean) on the normalized Intensity are therefore decreasing with N as $N^{-1/2}$ (**Fig. SI5**). To get a RSE below 2%, N=20-25 spheroids are necessary for an analysis up to 60 µm from the periphery. For deep layers, a larger number of spheroids are needed to reach sur RSE (N=70 spheroids for 80 µm from the periphery). Hence a minimum of N=30 spheroids is recommended to get reliable results at an imaging depth corresponding to the first quarter of the spheroids. This number rises up to N=70 spheroids for an accurate analysis close to the equatorial plane.

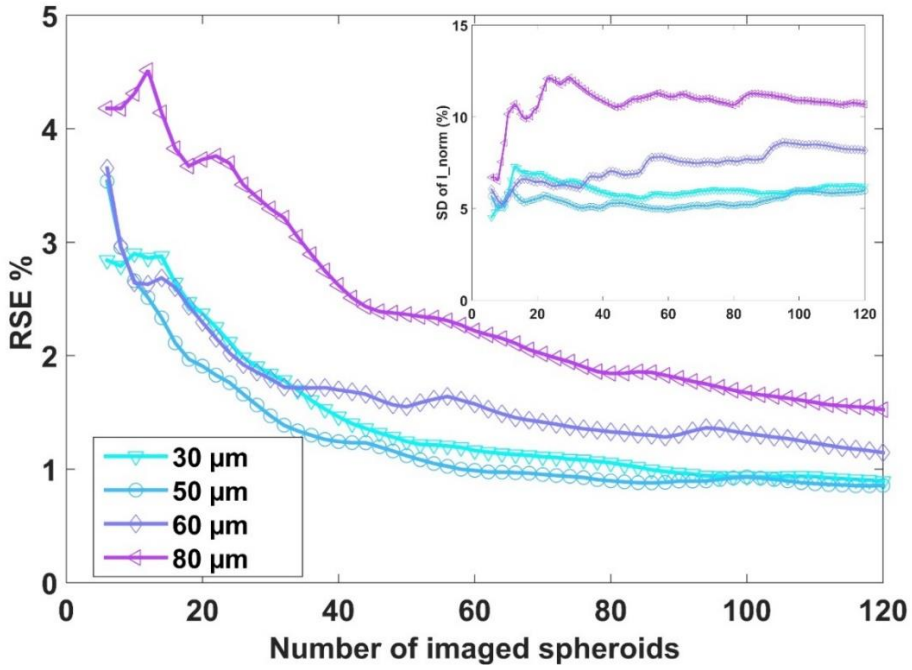

Figure SI 5. Error analysis due to the number of spheroids analysed.

Relative Standard Error (RSE=SEM/mean) as a function of the number of spheroids for different distance from the periphery (30 µm (cyan, triangles pointing down), 50 µm (light blue, circles), 60 µm (intense blue, diamonds) and 80 µm (purple, triangles pointing left). ***Inset:*** *Standard Deviation SD of the normalised Intensity I_norm as a function of the number of spheroids, for the same distance from the periphery.*

Figure SI 6. HCT116 cell incubated in 2D with nanoparticles and spheroid formation afterwards

To make a comparison between cellular uptake of AGuIX®-Cy5 nanoparticles in monolayer cells and multicellular spheroids, two parallel experiments have been done.

In the first experiment, HCT116 cells were seeded in agarose-based microwells (**Fig. SI 6A, Step I**) and after 48h were exposed to AGuIX®-Cy5 nanoparticles for 24h (**Fig. SI 6A, Step II**) followed by fixation (**Fig. SI 6A, Step III**).

In the other experiment HCT116 monolayer cells that were exposed to AGuIX®-Cy5 nanoparticles for 24h (**Fig. SI 6B, Step I**) were seeded in agarose-based microwells to allow spheroid formation (**Fig. SI 6B, Step II**). After 72h, these spheroids were fixed (**Fig. SI 6B, Step III**).

Spheroids from both experiment were clarified with glycerol 80% (**Fig. SI 6, Step III**) and imaged via confocal microscopy. The confocal images of these two experiments and orthogonal view of spheroids demonstrate that when spheroids are incubated with nanoparticles, clusters could be observed evenly in extracellular and intracellular regions of spheroids and nanoparticles clusters are more in peripheral region than in the centre (**Fig. SI 6A**). When spheroids are made from already AGuIX®-Cy5 labelled cells, only sparse clusters, with a scattered distribution are observed in spheroids (**Fig. SI 6B)**.

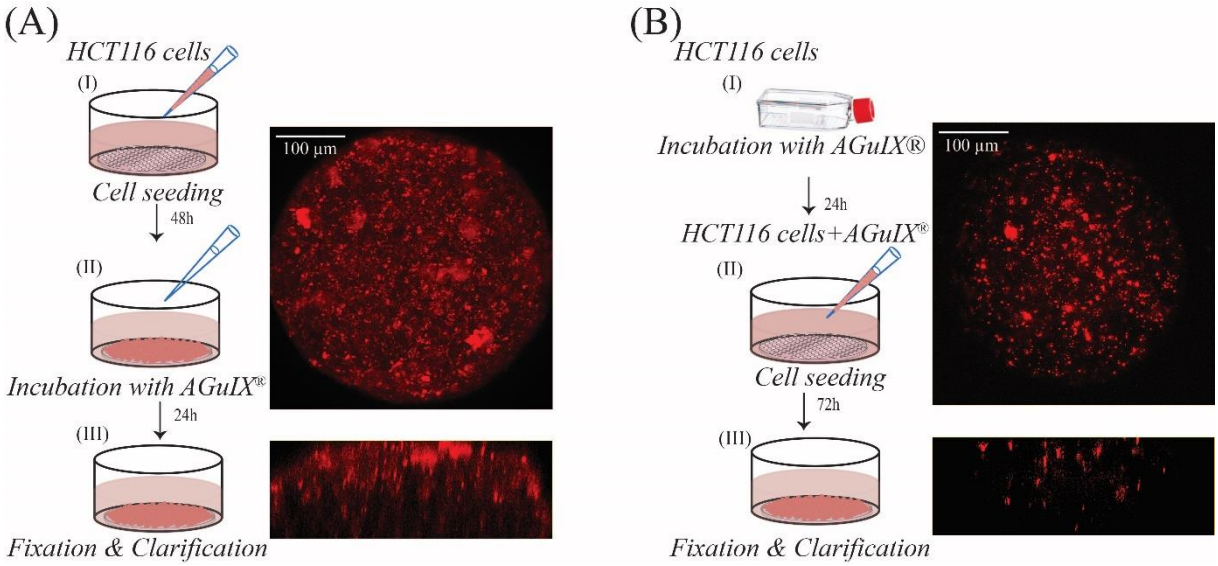

Figure SI. 6. ***Difference in distribution of AGuIX® nanoparticles in HCT116 multicellular tumour spheroids incubated in 2D and 3D cell culture.***

*(A) Spheroids were prepared with agarose-based microwells and were (**Step I**) and after 48h exposed to 2mM AGuIX® nanoparticles for 24h **(step II)** and were fixed and clarified **(Step III)** and imaged with confocal microscopy. (B) Monolayer HCT116 cells were incubated with 2mM AGuIX® nanoparticles for 24h **(Step I)** and then HCT116 spheroids were prepared with these cells **(step II)** and spheroids were fixed, clarified **(Step III)** and imaged with confocal microscopy.*

Figure SI 7. nanoscale Secondary Ion Mass Spectrometry control analysis

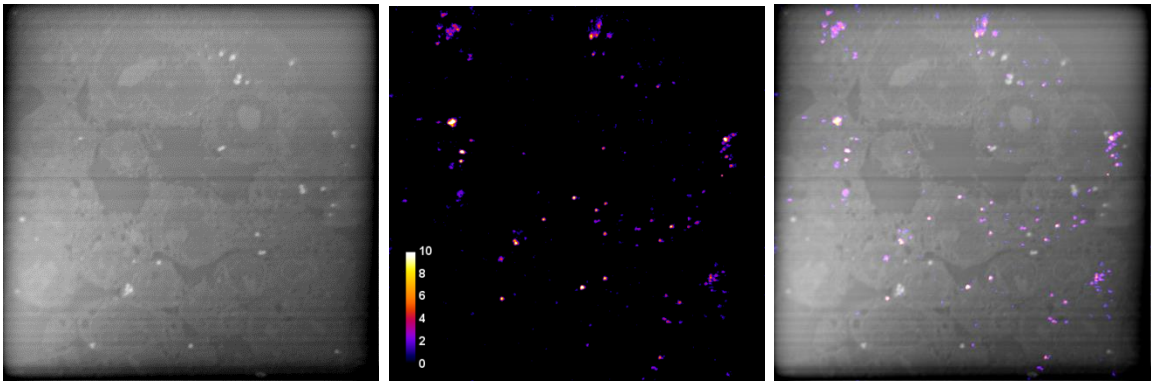

A B C

Figure SI. 7.

(A) *NanoSIMS image of $^{12}C^-$ of the same area as in* ***Figure 5*** *provides the proof of the entirety of the section. The slight contrast is due to the compositional variation of different cells compartments and the surrounding resin (the actual contrast is much lower). A few spots with unusually high $^{12}C^-$ emission are probably location of vacuoles.* ***(B)*** *recalled of the distribution of AGuiX-Cy5 nanoparticles.* ***(C)*** *Merged image of $^{28}Si^-$ and $^{12}C^-$. Image field: 60 µm.*

References

1 S. Hua, M. B. C. de Matos, J. M. Metselaar and G. Storm, *Front. Pharmacol.*, 2018, **9**, 1–14.

2 L. J. Bray, D. W. Hutmacher and N. Bock, *Front. Bioeng. Biotechnol.*, 2019, **7**, 1–36.

3 S. E. Gould, M. R. Junttila and F. J. De Sauvage, *Nat. Med.*, 2015, **21**, 431–439.

4 G. Lazzari, P. Couvreur and S. Mura, *Polym. Chem.*, 2017, **8**, 4947–4969.

5 A. Sontheimer-Phelps, B. A. Hassell and D. E. Ingber, *Nat. Rev. Cancer*, 2019, **19**, 65–81.

6 S. Peel, A. M. Corrigan, B. Ehrhardt, K. J. Jang, P. Caetano-Pinto, M. Boeckeler, J. E. Rubins, K. Kodella, D. B. Petropolis, J. Ronxhi, G. Kulkarni, A. J. Foster, D. Williams, G. A. Hamilton and L. Ewart, *Lab Chip*, 2019, **19**, 410–421.

7 D. Peer, J. M. Karp, S. Hong, O. C. Farokhzad, R. Margalit and R. Langer, *Nat. Nanotechnol.*, 2007, **2**, 751–760.

8 D. Rosenblum, N. Joshi, W. Tao, J. M. Karp and D. Peer, *Nat. Commun.*, , DOI:10.1038/s41467-018-03705-y.

9 M. Zanoni, F. Piccinini, C. Arienti, A. Zamagni, S. Santi, R. Polico, A. Bevilacqua and A. Tesei, *Sci. Rep.*, 2016, **6**, 1–11.

10 S. Wilhelm, A. J. Tavares, Q. Dai, S. Ohta, J. Audet, H. F. Dvorak and W. C. W. Chan, *Nat. Rev. Mater.*, 2016, **1**, 16014.

11 E. J. Guggenheim, S. Milani, P. J. F. Röttgermann, M. Dusinska, C. Saout, A. Salvati, J. O. Rädler and I. Lynch, *NanoImpact*, 2018, **10**, 121–142.

12 W. Asghar, R. El Assal, H. Shafiee, S. Pitteri, R. Paulmurugan and U. Demirci, *Mater. Today*, 2015, **18**, 539–553.

13 S. Nath and G. R. Devi, *Pharmacol. Ther.*, 2016, 163, 94–108.

14 M. Millard, I. Yakavets, V. Zorin, A. Kulmukhamedova, S. Marchal and L. Bezdetnaya, *Int. J. Nanomedicine*, 2017, **Volume 12**, 7993–8007.

15 F. Hirschhaeuser, H. Menne, C. Dittfeld, J. West, W. Mueller-klieser and L. A. Kunz-schughart, *J. Biotechnol.*, 2010, **148**, 3–15.

16 H. L. Ma, Q. Jiang, S. Han, Y. Wu, J. C. Tomshine, D. Wang, Y. Gan, G. Zou and X. J. Liang, *Mol. Imaging*, 2012, **11**, 487–498.

17 S. Huo, H. Ma, K. Huang, J. Liu, T. Wei, S. Jin, J. Zhang, S. He and X. J. Liang, *Cancer Res.*, 2013, **73**, 319–330.

18 A. Virgone-Carlotta, M. Lemasson, H. C. Mertani, J. J. Diaz, S. Monnier, T. Dehoux, H. Delanoë-Ayari, C. Rivière and J. P. Rieu, *PLoS One*, , DOI:10.1371/journal.pone.0188100.

19 B. Rodday, F. Hirschhaeuser, S. Walenta and W. Mueller-Klieser, *J. Biomol. Screen.*, 2011, **16**, 1119–1124.

20 J. M. Kelm, N. E. Timmins, C. J. Brown, M. Fussenegger and L. K. Nielsen, *Biotechnol. Bioeng.*, 2003, **83**, 173–180.

21 Y.-C. Chen, P. N. Ingram, S. Fouladdel, S. P. McDermott, E. Azizi, M. S. Wicha and E. Yoon, *Sci. Rep.*, 2016, **6**, 27301.

22 M. Akay, J. Hite, N. G. Avci, Y. Fan, Y. Akay, G. Lu and J. J. Zhu, *Sci. Rep.*, 2018, **8**, 1–9.

23 R. Mukhopadhyay, *Anal. Chem.*, 2007, **79**, 3249–3253.

24 B. J. van Meer, H. de Vries, K. S. A. Firth, J. van Weerd, L. G. J. Tertoolen, H. B. J. Karperien, P. Jonkheijm, C. Denning, A. P. IJzerman and C. L. Mummery, *Biochem. Biophys. Res. Commun.*, 2017, **482**, 323–328.

25 M. W. Toepke and D. J. Beebe, *Lab Chip*, 2006, **6**, 1484–1486.

26 D. T. Butcher, T. Alliston and V. M. Weaver, *Nat. Rev. Cancer*, 2009, **9**, 108–22.

27 J. M. Lee, D. Y. Park, L. Yang, E. J. Kim, C. D. Ahrberg, K. B. Lee and B. G. Chung, *Sci. Rep.*, 2018, **8**, 1–10.

28 Y. Li and E. Kumacheva, *Sci. Adv.*, 2018, 4, 1–11.

29 X. Gong, C. Lin, J. Cheng, J. Su, H. Zhao, T. Liu, X. Wen and P. Zhao, *PLoS One*, 2015, **10**, e0130348.

30 J. Dahlmann, G. Kensah, H. Kempf, D. Skvorc, A. Gawol, D. A. Elliott, G. Dräger, R. Zweigerdt, U. Martin and I. Gruh, *Biomaterials*, 2013, **34**, 2463–2471.

31 D. L. Priwitaningrum, J. B. G. Blondé, A. Sridhar, J. van Baarlen, W. E. Hennink, G. Storm, S. Le Gac and J. Prakash, *J. Control. Release*, 2016, **244**, 257–268.
32 G. Fang, H. Lu, A. Law, D. Gallego-Ortega, D. Jin and G. Lin, *Lab Chip*, 2019, 23–25.
33 X. Hu, X. Hu, S. Zhao, S. Zhao, Z. Luo, Y. Zuo, Y. Zuo, F. Wang, F. Wang, J. Zhu, J. Zhu, L. Chen, L. Chen, D. Yang, Y. Zheng, Y. Zheng, Y. Cheng, F. Zhou, Y. Yang and Y. Yang, *Lab Chip*, 2020, **20**, 2228–2236.
34 V. Normand, D. L. Lootens, E. Amici, K. P. Plucknett and P. Aymard, *Biomacromolecules*, 2000, **1**, 730–738.
35 T. H. Jovic, G. Kungwengwe, A. C. Mills and I. S. Whitaker, *Front. Mech. Eng.*, 2019, **5**, 19.
36 A. Pluen, P. A. Netti, R. K. Jain and D. A. Berk, *Biophys. J.*, 1999, **77**, 542–52.
37 F. Lux, V. L. Tran, E. Thomas, S. Dufort, F. Rossetti, M. Martini, C. Truillet, T. Doussineau, G. Bort, F. Denat, F. Boschetti, G. Angelovski, A. Detappe, Y. Crémillieux, N. Mignet, B. T. Doan, B. Larrat, S. Meriaux, E. Barbier, S. Roux, P. Fries, A. Müller, M. C. Abadjian, C. Anderson, E. Canet-Soulas, P. Bouziotis, M. Barberi-Heyob, C. Frochot, C. Verry, J. Balosso, M. Evans, J. Sidi-Boumedine, M. Janier, K. Butterworth, S. Mcmahon, K. Prise, M. T. Aloy, D. Ardail, C. Rodriguez-Lafrasse, E. Porcel, S. Lacombe, R. Berbeco, A. Allouch, J. L. Perfettini, C. Chargari, E. Deutsch, G. Le Duc and O. Tillement, *Br. J. Radiol.*, 2019.
38 W. Rima, L. Sancey, M. T. Aloy, E. Armandy, G. B. Alcantara, T. Epicier, A. Malchère, L. Joly-Pottuz, P. Mowat, F. Lux, O. Tillement, B. Burdin, A. Rivoire, C. Boulé, I. Anselme-Bertrand, J. Pourchez, M. Cottier, S. Roux, C. Rodriguez-Lafrasse and P. Perriat, *Biomaterials*, 2013, **34**, 181–195.
39 G. Le Duc, S. Roux, A. Paruta-Tuarez, S. Dufort, E. Brauer, A. Marais, C. Truillet, L. Sancey, P. Perriat, F. Lux and O. Tillement, *Cancer Nanotechnol.*, 2014, **5**, 1–14.
40 L. Le Roux, A. Volgin, D. Maxwell, K. Ishihara, J. Gelovani and D. Schellingerhout, *Mol. Imaging*, 2008, **7**, 214–221.
41 J. F. Dekkers, M. Alieva, L. M. Wellens, H. C. R. Ariese, P. R. Jamieson, A. M. Vonk, G. D. Amatngalim, H. Hu, K. C. Oost, H. J. G. Snippert, J. M. Beekman, E. J. Wehrens, J. E. Visvader, H. Clevers and A. C. Rios, *Nat. Protoc.*, 2019, **14**, 1756–1771.
42 T. Silva Santisteban, O. Rabajania, I. Kalinina, S. Robinson and M. Meier, *Lab Chip*, 2018, **18**, 153–161.
43 E. Nürnberg, M. Vitacolonna, J. Klicks, E. von Molitor, T. Cesetti, F. Keller, R. Bruch, T. Ertongur-Fauth, K. Riedel, P. Scholz, T. Lau, R. Schneider, J. Meier, M. Hafner and R. Rudolf, *Front. Mol. Biosci.*, 2020, **7**, 1–19.
44 J. L. Guerquin-Kern, T. Di Wu, C. Quintana and A. Croisy, *Biochim. Biophys. Acta - Gen. Subj.*, 2005, **1724**, 228–238.
45 G. Slodzian, B. Daigne, F. Girard, F. Boust and F. Hillion, *Biol. Cell*, 1992, **74**, 43–50.
46 C. A. Schneider, W. S. Rasband and K. W. Eliceiri, *Nat. Methods*, 2012, **9**, 671–675.
47 C. Messaoudil, T. Boudier, C. O. S. Sorzano and S. Marco, *BMC Bioinformatics*, 2007, **8**, 1–9.
48 M. Singh, D. A. Close, S. Mukundan, P. A. Johnston and S. Sant, *Assay Drug Dev. Technol.*, 2015, **13**, 570–583.
49 L. B. Sims, L. T. Curtis, H. B. Frieboes and J. M. Steinbach-Rankins, *J. Nanobiotechnology*, 2016, **14**, 1–12.
50 A. R. Kang, H. I. Seo, B. G. Chung and S. H. Lee, *Nanomedicine Nanotechnology, Biol. Med.*, 2015, **11**, 1153–1161.
51 FR 1870349, .
52 L. Štefančíková, E. Porcel, P. Eustache, S. Li, D. Salado, S. Marco, J. L. Guerquin-Kern, M. Réfrégiers, O. Tillement, F. Lux and S. Lacombe, *Cancer Nanotechnol.*, 2014, **5**, 1–15.
53 L. Sancey, F. Lux, S. Kotb, S. Roux, S. Dufort, A. Bianchi, Y. Crémillieux, P. Fries, J.-L. Coll, C. Rodriguez-Lafrasse, M. Janier, M. Dutreix, M. Barberi-Heyob, F. Boschetti, F. Denat, C. Louis, E. Porcel, S. Lacombe, G. Le Duc, E. Deutsch, J.-L. Perfettini, A. Detappe, C. Verry, R. Berbeco, K. T. Butterworth, S. J. McMahon, K. M. Prise, P. Perriat and O. Tillement, *Br. J. Radiol.*, 2014, **87**, 20140134.

54 T. Stylianopoulos, L. L. Munn and R. K. Jain, *Trends in Cancer*, 2018, **4**, 292–319.
55 K. Carver, X. Ming and R. L. Juliano, *Mol. Ther. - Nucleic Acids*, 2014, **3**, e153.
56 H. Kang, S. Mintri, A. V. Menon, H. Y. Lee, H. S. Choi and J. Kim, *Nanoscale*, 2015, **7**, 18848–18862.
57 K. Raza, P. Kumar, N. Kumar and R. Malik, *Pharmacokinetics and biodistribution of the nanoparticles*, Elsevier Ltd, 2017.
58 J. Kondo, T. Ekawa, H. Endo, K. Yamazaki, N. Tanaka, Y. Kukita, H. Okuyama, J. Okami, F. Imamura, M. Ohue, K. Kato, T. Nomura, A. Kohara, S. Mori, S. Dan and M. Inoue, *Cancer Sci.*, 2019, **110**, 345–355.
59 S. E. Park, A. Georgescu and D. Huh, *Science (80-.).*, 2019, **364**, 960–965.
60 A. Ahmed, S. Goodarzi, C. Frindel, G. Recher, C. Riviere and D. Rousseau, *in revision.*
61 A. Prunet, S. Lefort, H. Delanoë-Ayari, B. Laperrousaz, G. Simon, C. Barentin, S. Saci, F. Argoul, B. Guyot, J.-P. Rieu, S. Gobert, V. Maguer-Satta and C. Rivière, *Lab Chip*, 2020, 27–32.
62 I. F. Rizzuti, P. Mascheroni, S. Arcucci, Z. Ben-Mériem, A. Prunet, C. Barentin, C. Rivière, H. Delanoë-Ayari, H. Hatzikirou, J. Guillermet-Guibert and M. Delarue, *Phys. Rev. Lett.*, 2020, **125**, 128103.
63 A. Albanese, A. K. Lam, E. A. Sykes, J. V. Rocheleau and W. C. W. Chan, *Nat. Commun.*, 2013, **4**, 1–8.
64 T. Yu, J. Zhu, Y. Li, Y. Ma, J. Wang, X. Cheng, S. Jin, Q. Sun, X. Li, H. Gong, Q. Luo, F. Xu, S. Zhao and D. Zhu, *Sci. Rep.*, 2018, **8**, 1–9.